(NASA-TM-X-70383) FEASIBILITY STUDY OF A SWEPT FREQUENCY ELECTROMAGNETIC PROBE (SWEEP) USING INDUCTIVE COUPLING FOR THE DETERMINATION OF SUBSURFACE (Massachusetts Inst. of Tech.) 111 p HC $8.75 G3/13

N74-34789

Unclas 51047

Feasibility study of a swept frequency electromagnetic probe (SWEEP) using inductive coupling for the determination of subsurface conductivity of the earth and water prospecting in arid regions.

(CSR TR 74-3)

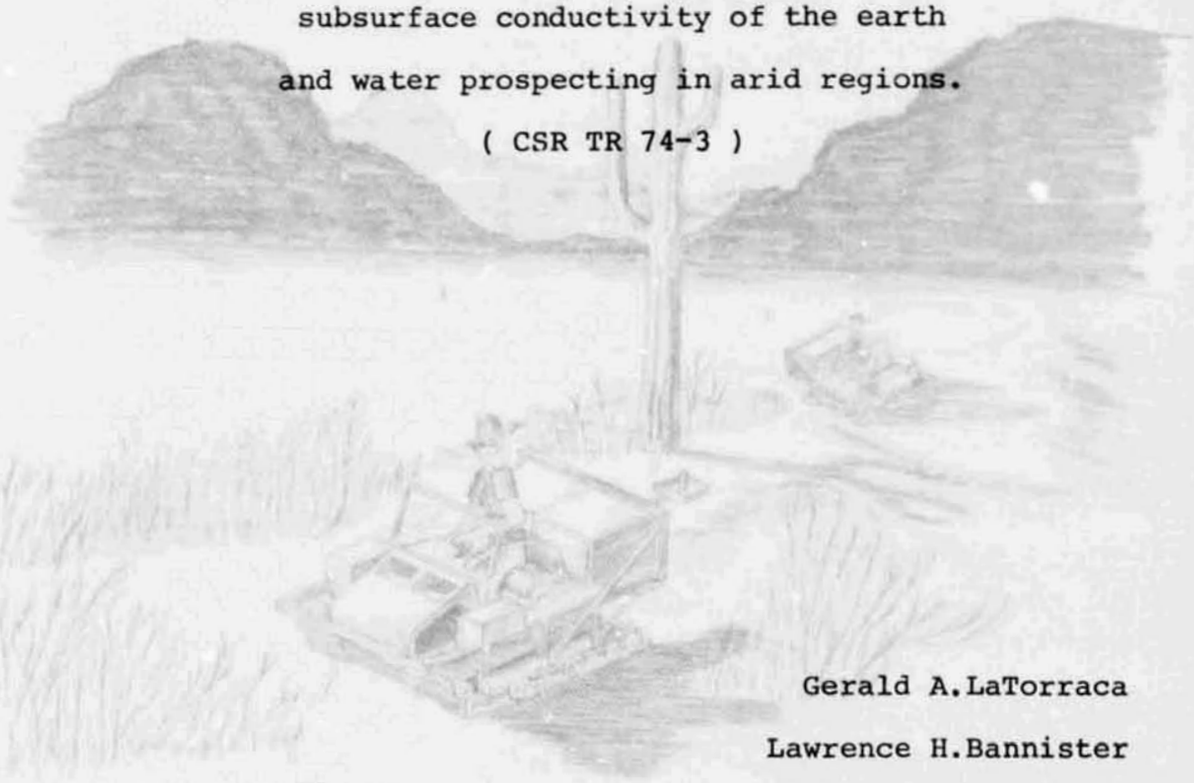

Gerald A.LaTorraca

Lawrence H.Bannister

September 1974

Jointly sponsored by

CENTER FOR SPACE RESEARCH

and TECHNOLOGY ADAPTATION PROGRAM,

MASSACHUSETTS INSTITUTE OF TECHNOLOGY

NASA grant p.80

PREFACE

A fortuitous set of circumstances brought together a group of people with diverse interests to address the important problem of finding ground water. It appeared that techniques developed for electromagnetic probing of the lunar interior, and techniques developed for the generation of high power audio frequencies, could be combined to make practical a magnetic inductive coupling system for the rapid measurement of ground conductivity profiles which are very helpful when prospecting for the presence and quality of subsurface water.

Thus, we undertook the study and conceptual design of the system described herein which involves the measurement of the direction, intensity, and time phase of the magnetic field observed near the surface of the earth at a distance from a horizontal coil energized so as to create a field that penetrates the earth. From such observations, we planned to deduce the conductivity and stratification of the subsurface.

As a result of our theoretical studies and a rudimentary experiment in an arid region we now can show that the approach is conceptually valid and that this geophysical prospecting technique deserves to be developed into a pragmatic system for the economical exploration of subterranean water resources.

TABLE OF CONTENTS

LIST OF ILLUSTRATIONS

LIST OF ILLUSTRATIONS (CONTINUED)

1.0 Summary

A geophysical probing technique, which we call SWEEP, based on a measurement of the inductive coupling between two coils deployed on, or near, the surface of the earth has been developed as an extension of earlier work. One coil is energized with an alternating current and the other is used as a means of measuring the apparent magnetic field at a distance. Because the system requires no physical contact with the ground, and because many different frequencies are used, the inductive technique avoids many of the problems, and resolves many of the ambiguities, inherent in other geophysical probing techniques.

The SWEEP inductive coupling technique shows promise as a means whereby subsurface conductivity can be measured quickly, easily, and inexpensively. And, because subterranean water causes contrasts in subsurface conductivity, this technique shows promise as a useful tool for the detection of ground water in arid regions.

Using a collection of available equipment, a field trial was conducted in an arid region near El Paso, Texas, to test the validity of the concept and the feasibility of making an automated system for the measurement of ground conductivity. In this field trial, a coil comprising twelve turns of #10 wire was laid on the ground in the form of a square with a side of 25 meters. This coil was energized with alternating current in the audio frequency range with various power sources ranging from three kilowatts at the lowest frequency of 60 hertz to ten milliwatts at the highest frequency of 20 kilohertz. The resultant magnetic field was measured at distances from the source of 20 meters to 500 meters, using a manually transported coil having 1200 turns with a cross-sectional area of one square

meter; this coil being arranged so that it could be rotated mechanically to either a horizontal or vertical position. A phase locked loop voltmeter was used to measure the magnitude and phase of the observed vertical and horizontal magnetic field components.

Using extensions of prior theoretical analyses and a computer implemented model, we have been able to achieve an interpretation of the experimental data that agrees well with geological conditions of the field sites determined previously by much more laborious techniques. Specifically, our interpretation yields an indication that at one test site there is a water bearing stratum nine meters below the surface of the earth, and at the other test site there is a water bearing stratum at a depth of 100 meters. These results agree with the depths at which water is found in nearby existing wells.

To provide the feasibility demonstration described in this report, we used crude hardware, considerable manual labor during the field experiment, and lengthy calculations utilizing a large computer facility. However, with the knowledge gained through the development of our measurement and interpretation techniques, we feel that no further major technological advances are required to implement an automated system that would permit the economical mapping of subsurface conditions in arid regions at depths less than a few hundred meters.

Conceptually, the ultimate SWEEP system would comprise two small instrumented vehicles, one carrying a horizontal source coil and a high power audio frequency generator, the other carrying a receiving coil and a coherent detector. Data could be interpreted in real time in the field, and since there is no requirement for physical contact with the

ground, both vehicles could be maneuvered to permit rapid and economical mapping of large areas. The feasibility study and experiments reported here demonstrate that this concept is viable and realistic.

2.0 Introduction

The geophysical prospecting technique reported here involves the measurement of the complex inductive coupling between two coils deployed on or near the surface of the earth. A source coil, deployed horizontally, is energized with currents of the order of several amperes at frequencies ranging from a few hertz to a few kilohertz. A detecting coil, oriented alternately horizontally and vertically, at distances up to several hundred meters, is used in the measurement of the magnitude and phase of the field created just above the surface of the earth. Inversion of these data then yields a measure of the subsurface conductivity.

Like other electrical prospecting methods, the SWEEP procedure measures electrical conductivity as a function of depth. And, because electrical conductivity of rocks and sediments depends strongly on the porosity, the amount of saturation, and the electrical conductivity of the pore-fluids, this conductivity data may be interpreted in terms of the presence or absence of water.

The low frequency inductive technique promises several major advantages over other electrical prospecting techniques. First, a properly instrumented system is likely to be much faster to operate than existing techniques because there is no necessity for electrical contact with the ground and data can be collected while an instrumented vehicle is moving. Second, the alternating current frequency, which is one of the prime system variables, can be swept automatically so that a large amount of data can be collected rapidly without manual intervention. And, third, the problems associated with highly conductive layers near the surface, which may

be a severe handicap with other techniques, can be overcome by using a set of frequencies such that the surface layer is essentially transparent but the underlying strata can be delineated clearly.

Further, and importantly, interpretation of data collected with the low frequency inductive technique promises to be less ambiguous than interpretation of data collected with existing techniques. In common with seismic sounding and electrical resistivity methods, the distance between the source and detecting elements is an independent variable. But, additionally, with the inductive coupling method, signal frequency is an independent variable. This additional degree of freedom makes it possible to collect a wealth of semi-redundant data that can be used to resolve experimental errors and uncertainties. And, because the SWEEP procedure promises to be fast and economical, one can make many traverses in different directions to distinguish between vertical and lateral variations in conductivity.

2.1 Background

Several seemingly unrelated developments and observations coalesced in a decision to undertake the feasibility study reported here.

In the MIT Apollo 17 Surface Electrical Properties Experiment, conducted successfully on the moon in December 1972, electromagnetic energy was radiated from a small radio transmitter and horizontal electric dipole deployed at the landing site. A receiver mounted on the Lunar Roving Vehicle measured, and recorded on a portable magnetic tape recorder, the resulting field strengths as a function of distance. By interpreting the interference patterns produced by the various waves that travelled above and below the lunar surface, it was possible to

determine some of the electrical characteristics of the lunar interior. One of the early objectives in the lunar experiment was to search for the presence of water in the subsurface of the moon. As a result of those measurements, it is now certain that at the Apollo 17 landing site, there is no free water at least to depths of several hundred meters.

Prospecting for subsurface water also has increased urgency here on earth. We are aware of the serious problem caused by the continuing drought in the Sahel region of West Africa. This region, including the countries of Mali, Upper Volta, Senegal, Mauritania, and the southern reaches of the Sahara Desert, is now in the sixth year of subnormal rainfall that has caused great deprivation and widespread famine. In the hope of helping to alleviate some of the problems, we explored the possibility of adapting the lunar technology and experience to the purpose of finding subsurface water in arid regions of the earth.

A direct transfer of the lunar technology is not feasible because, at the radio frequencies appropriate for an exploration of the lunar interior, the electrical losses in the earth are intolerably large.

However, considerable attention has been given in recent years to the diffusion through the earth of electromagnetic energy at very low frequencies for which the electrical losses can be very small. Several theoretical solutions for the fields produced by a loop in the presence of a layered conductive earth have been published. And experiments have been reported in which the conductivity of the subsurface was measured by observing the fields produced by a magnetic dipole at the surface. These experiments, for the most part, were handicapped by the difficulty of generating high power,

low frequency, signals with easily transportable apparatus.

As part of another program, attention has been directed recently to the design of a variable voltage, variable frequency, power supply useful for converting energy stored in batteries to the form required to drive an electric motor in an electric vehicle. Coincidentally, a switched source synthesizer technique inspired by this purpose can be adapted readily to the frequencies and power levels appropriate for the inductive coupling method of measuring subsurface conductivity of the earth.

So, the advent of a practical method for generating the required high power, variable frequency, source signals, the theoretical formulations describing the interaction of low frequency signals with the earth, the evident need for a prospecting technique permitting fast and economical survey of subsurface water resources in a large arid region of the earth, a considerable theoretical base result from a lunar experiment, and the practical implem.. ..on of the automated equipment used in the lunar experiment, combined to suggest that it would be worthwhile to examine the feasibility of an automated prospecting tool for use on earth.

The results of this feasibility study, reported here, are most encouraging.

3.0 The Experiment Concept

As with most remote sensing techniques, the fine detail of the rigorous analysis may be tedious and abstruse, but there is an intuitive approximation available that provides a powerful insight into the problem. In this section we describe the concept of the technique and give a physical explanation.

For the mathematically inclined reader, this section should provide a useful basis for the more mathematical section on theory. For the reader who is not mathematically inclined, this section should provide a good basis for understanding the method and he may wish to omit the later theoretical section.

Consider two coils in free space, such as shown schematically in Figure 3-1. One coil, the source, is energized with an alternating current. The other coil, the detector, is either coplanar with the source coil or it is perpendicular to the plane of the source coil and has its center on the plane defined by the source. With the source coil energized with an alternating current, there will be a time-varying magnetic field that can be detected by the other coil. With the configuration shown in Figure 3-1(a), the detecting coil that is oriented in the plane containing the source coil ("horizontally") will be maximally coupled to the time-varying field while the coil that is oriented orthogonal to the plane ("vertically") will be completely decoupled and unaffected by the time-varying field. Thus, at the terminals of the horizontal coil there will be an alternating voltage having a magnitude dependent on the distance between the source and detecting coils and the magnetic moment, or intensity, of the source coil. But no such voltage will exist at the terminals of the vertical

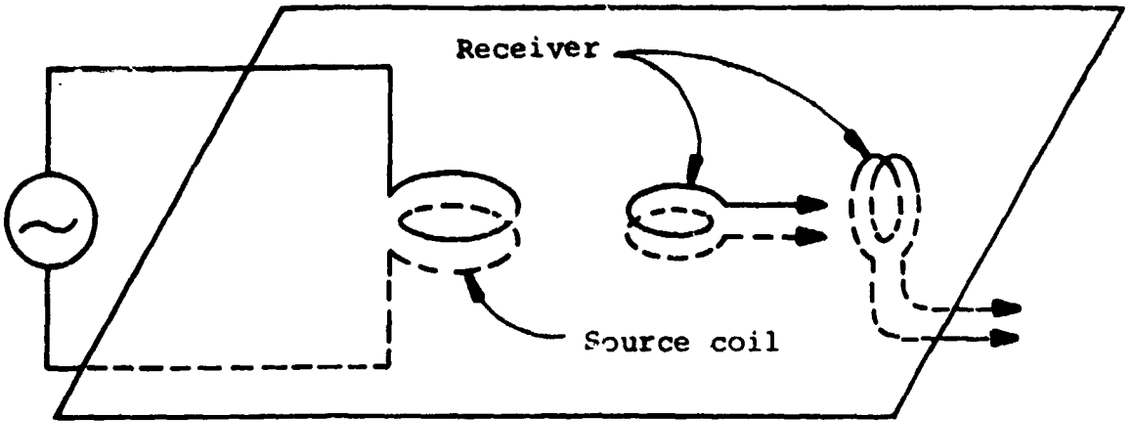

Figure 3-1(a). A Source Coil With Two Detecting Coils in the Same Plane

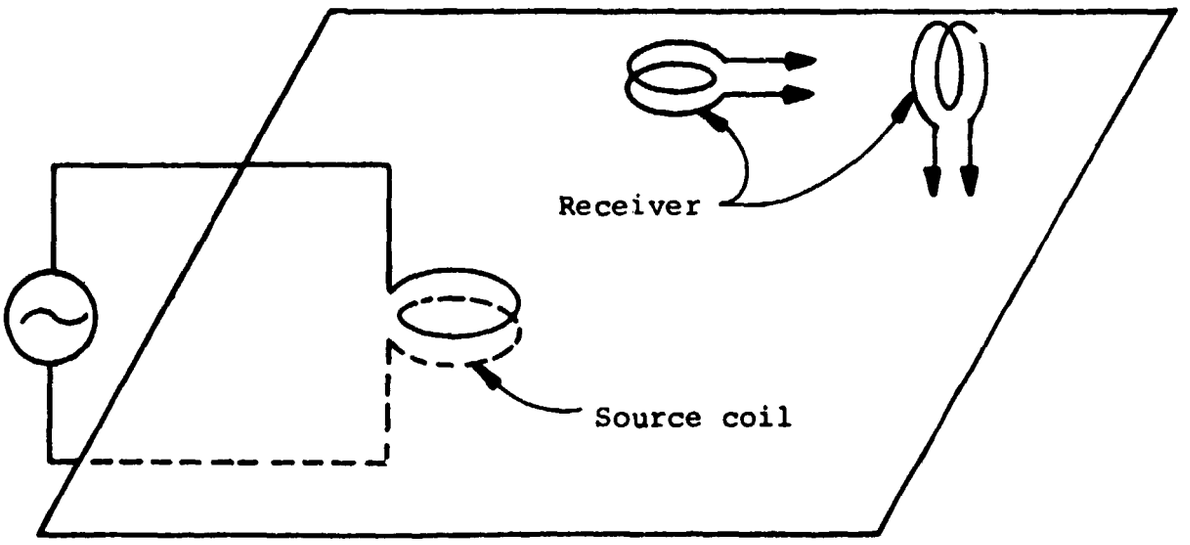

Figure 3-1(b). A Source Coil With Two Detecting Coils Displaced From the Plane

coil because, in free space, this coil is decoupled from the time-varying magnetic field.

If the detecting coils are displaced from the plane defined by the source coil, as in Figure 3-1(b), both coils will be coupled in varying degrees to the time-varying magnetic field and so an alternating voltage will appear at the terminals of both detecting coils. Calculation of the magnitude of these voltages is a straightforward geometrical problem for which the solution is well known.

If the two coils are not in free space but are near a conducting medium, then the magnetic field will not be symmetrical about the source coil but will be spatially distorted by an amount that depends on the conductivity of the medium. The practical situation is that which occurs when the source coil is laid flat on the surface of the earth. See Figure 3-2. The field is distorted because currents are induced in the conducting material by the source coil and these currents modify the spatial distribution of the magnetic field. Due to this distortion, both detecting coils will yield an output voltage that depends on the nature of the medium on each side of the interfacial plane.

The effect of this distortion can be visualized readily on the basis of a mathematically equivalent image of the source coil. The exact description of the image includes information on location, intensity, and time phase which are so adjusted that the superposition of the free-space field originating from the source coil and the hypothetical field arising from the image combine at the detector location to describe correctly the intensity, direction, and time dependence of the actual field. This image concept is illustrated in Figure 3-3 and the mathematical basis is described in Appendix D.

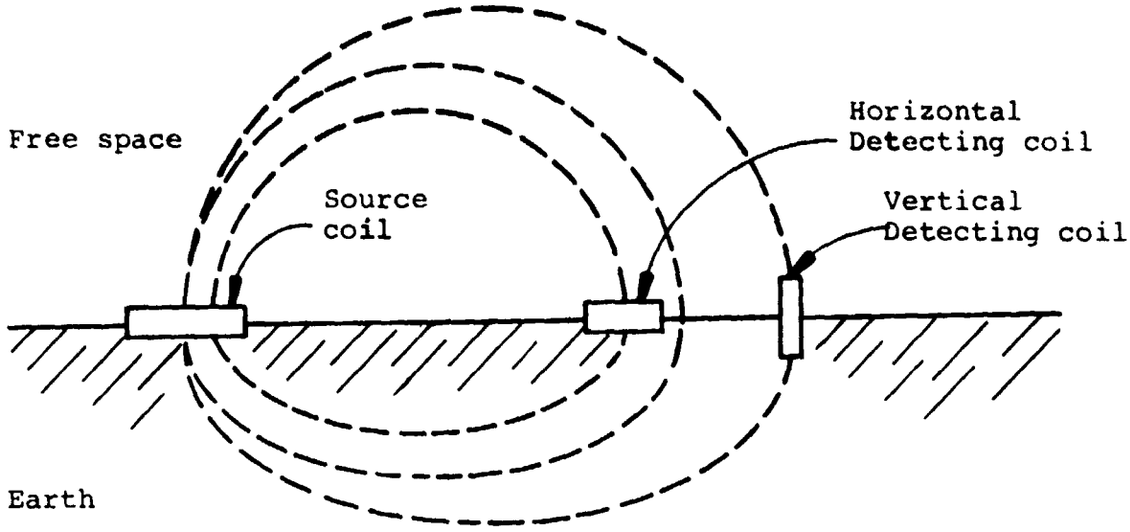

Figure 3-2. Distorted Magnetic Field Resulting from Presence of a Conducting Material.

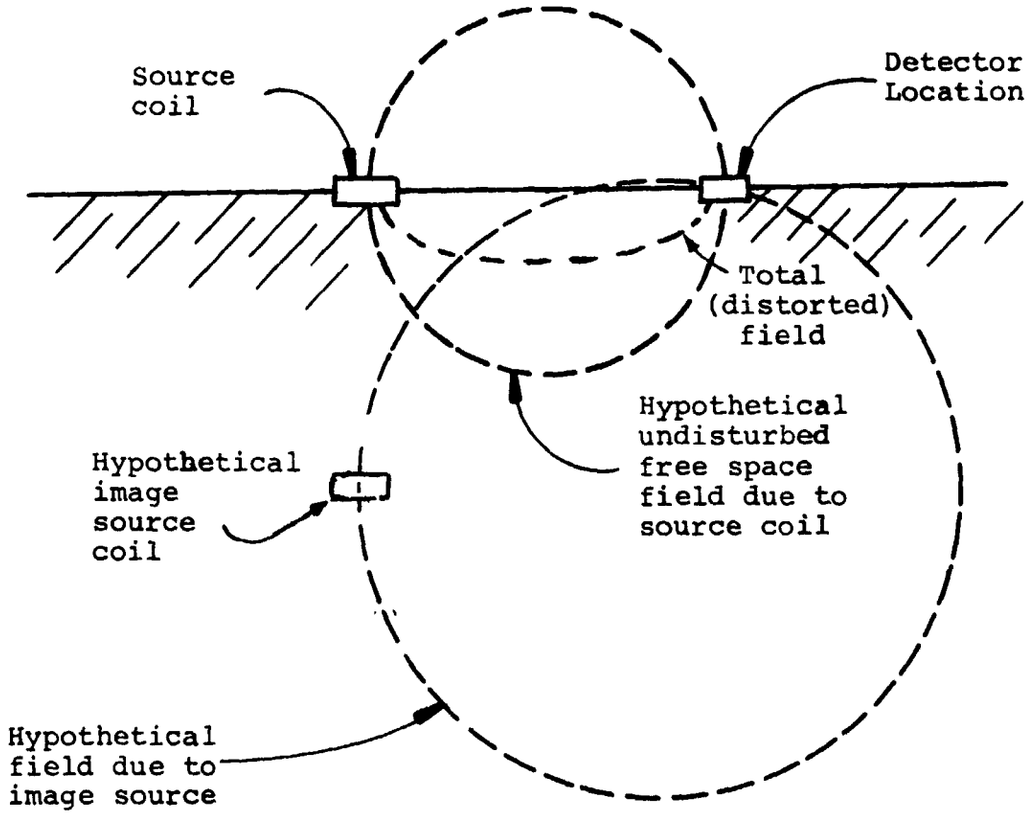

Figure 3-3. The Image Concept.

In actual practice, the situation is somewhat more complicated than the simple pictures of Figures 3-2 and 3-3 might indicate because the presence of a conducting material not only affects the spatial distribution of the magnetic field but also affects the time phase of the field relative to that which would occur in a free-space environment. However, this can be accounted for by associating a time phase with the image coil so that the time dependent phase of the hypothetical field associated with the image source is different from the phase of the free-space field associated with the original source coil.

The situation of interest to us is still more complicated because the earth is not a homogeneous body with one conductivity but generally consists of successive strata having different conductivities that are determined mainly by porosity and water salinity. Indeed, it is this layered structure and moisture dependent conductivity that we rely on to indicate the presence of subsurface water.

Figure 3-4 illustrates the simplest, idealized, model. If the first subsurface layer has zero conductivity, that is, it is an infinitely resistive insulator, then no currents will exist in this layer. But if the second layer consists of water saturated rock that is highly conductive, that is, it is a relatively low resistance conductor, then the source magnetic field will induce substantial currents in the second layer. These currents, in turn, will create a magnetic field which, viewed from the surface, will appear to have originated from an image coil located at some complex depth.

Although the image description of the magnetic field is a powerful conceptual tool, its application to the data analysis, as shown in Appendix D, is limited to large source-receiver separations. Since most of our data was

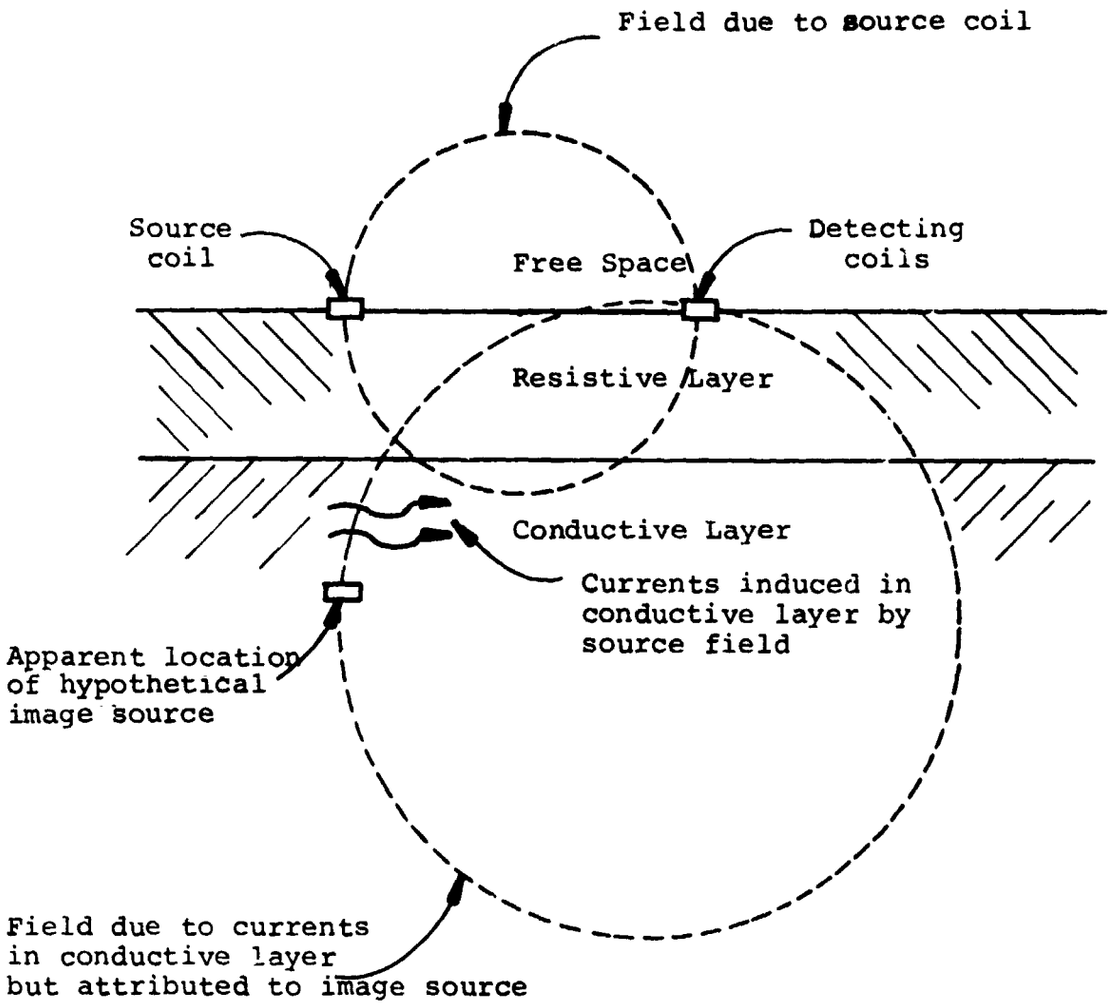

Figure 3-4. The Image Concept for the Two Layered Case

obtained at separations where the image formulation was invalid, we were forced to use a more exact integral formulation of the magnetic field. In the next section we shall describe the mathematical techniques used to formulate expressions for the magnetic field of a horizontal source loop on the surface of a multilayered earth.

4.0 Theoretical Analysis

In this section, we shall derive expressions for the magnetic fields induced by a horizontal current loop over a multilayer conducting earth in order to provide a theoretical basis for the analysis of the El Paso field measurements described in the subsequent chapters.

We shall assume:

a) a multilayered flat conductive earth,
b) the permeability (μ) of the earth is that of free space (μ_0),
c) displacement currents can be ignored (i.e., the quasistatic approximation holds),
d) the horizontal current loop can be approximated as a vertical magnetic dipole of moment m (i.e., a point source),
e) conductivity varies only with depth,
and f) the current varies sinusoidally with time, with an implied $e^{-i\omega t}$ time dependence in all expressions.

The current source is placed on the surface of the earth (h=o) and at the origin of a cylindrical set of coordinates with our observation point P at (r,z) as illustrated in Figure 4-1.

4.1 Magnetic Hertz Potential

To simplify the analysis of electromagnetic boundary value problems, "gauge functions" are defined in terms of the measurable fields, the electric field vector E (volts/meter) and the magnetic field intensity vector H (amperes/meter). The gauge we use for the current loop source is the magnetic Hertz vector Π which is expressed in terms of E and H as:

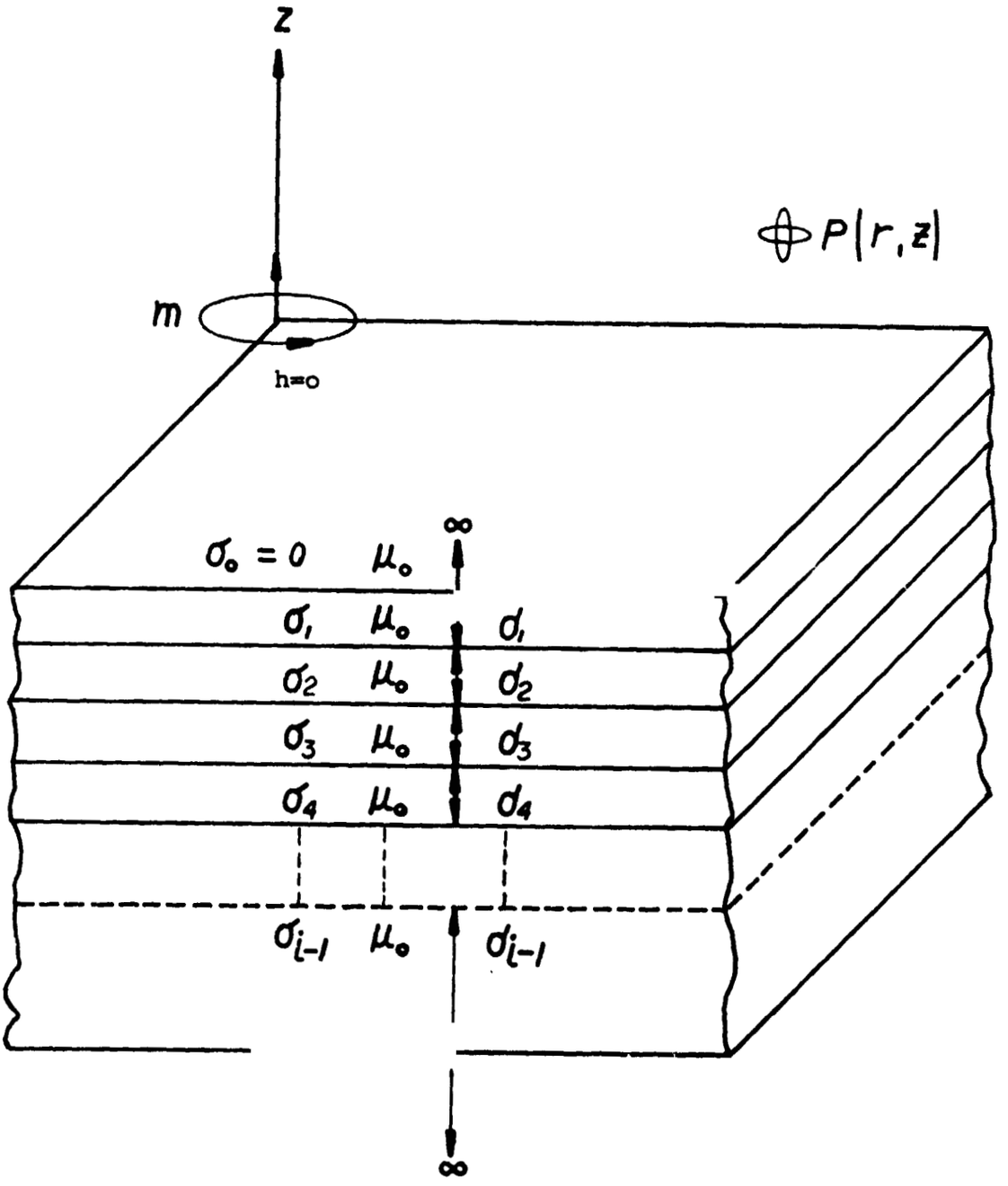

Figure 4-1. Geologic Model and Experiment Geometry

$$H = \cdot(\nabla \times \nabla \times \Pi) \tag{4.1A}$$

$$E = i\omega\mu(\nabla \times \Pi) \quad (e^{-i\omega t} \text{ time dependence implied}) \tag{4.1B}$$

The Hertz potential for a magnetic dipole is vertical. Therefore, the Helmholtz equation in layer 0 may be written in cylindrical coordinates as:

$$\nabla^2\Pi_{0z} + k^2\Pi_{0z} = -m\delta(R) \tag{4.2}$$

where:

$$\delta(R) = \frac{1}{2\pi}\int_0^\infty J_0(\lambda r)\lambda\, d\lambda \tag{4.3}$$

In the lower (source free) layers, we can write:

$$(\nabla^2 + k_i^2)\Pi_{iz} = 0 \tag{4.4}$$

where $k_i^2 = (i\sigma_i\mu_0\omega - \varepsilon_i\mu_0\omega^2) \approx i\sigma_i\mu_0\omega$ (quasistatic approximation) and to determine the boundary conditions on Π, equation (4.1) can be written in the form:

$$\frac{\partial^2}{\partial z^2}\Pi_z = H_z;\ \frac{\partial^2}{\partial r\partial z}\Pi_z = H_r;\quad H_\phi = 0 \tag{4.5A}$$

$$-i\omega\mu\frac{\partial}{\partial r}\Pi_z = E_\phi;\quad E_r = E_z = 0 \tag{4.5B}$$

The application of the normal boundary conditions for E and H on the Hertz vector Π_z yields the constraints that Π_z and $\partial\Pi_z/\partial z$ are continuous across the layers. We can now solve the Helmholtz equation in each layer and apply the boundary conditions to find Π_z at the observation

point P(r,z) above the surface of the earth. From the solution for Π_z and equation (4.5), we can readily deduce expressions for our measured field components H_z and H_r. The homogeneous solution for Π_z is of the form:

$$(\Pi_z)_h = \frac{m}{4\pi} \int_0^\infty J_0(\lambda r) e^{-(\lambda^2 - k^2)^{\frac{1}{2}} z} F(\lambda)\, d\lambda \qquad (4.6A)$$

where $F(\lambda)$ is an arbitrary function of λ.

The particular solution of the Helmholtz equation is of the form:

$$(\Pi_z)_\rho = \frac{m e^{ikR}}{4\pi R} \qquad (4.6B)$$

which can be put in the Sommerfeld integral form:

$$(\Pi_z)_\rho = \frac{m e^{ikR}}{4\pi R} = \frac{m}{4\pi} \int_0^\infty \frac{\lambda}{\alpha} e^{-\alpha |z|} J_0(\lambda r)\, d\lambda \qquad (4.7)$$

where:

$$\alpha = (\lambda^2 - k^2)^{\frac{1}{2}}$$

Thus, the complete solution in layer 0, which contains the source and the observation point, is of the form:

$$\Pi_{0z} = \frac{m}{4\pi} \int_0^\infty J_0(\lambda r) \left[\frac{\lambda}{\alpha_0} e^{-\alpha_0 z} + f_0(\lambda) e^{-\alpha_0 z} \right] d\lambda \qquad (4.8)$$

Each lower layer expression except the last must have downward and upward diffusing terms representing transmitted and reflected waves.

4.2 Two Layer Case

Consider now the two layer case where the lower layer extends to infinity. We can write expressions for Π_{1z} and Π_{2z} for layers 1 and 2 in the forms:

$$\Pi_{1z} = \frac{m}{4\pi} \int_0^\infty J_0(\lambda r) \left[f_1(\lambda) e^{\alpha_1 z} + f_2(\lambda) e^{-\alpha_1 z} \right] d\lambda \qquad (4.9)$$

$$\Pi_{2z} = \frac{m}{4\pi} \int_0^\infty J_0(\lambda r) \left[f_3(\lambda) e^{\alpha_2 z} \right] d\lambda \qquad (4.10)$$

Now we can apply the boundary conditions

$$\Pi_{0z} = \Pi_{1z} \quad @ \; z = 0 \qquad (4.11\,A)$$

$$\Pi_{1z} = \Pi_{2z} \quad @ \; z = -d_1 \equiv -d \qquad (4.11\,B)$$

and

$$\frac{\partial \Pi_{0z}}{\partial z} = \frac{\partial \Pi_{1z}}{\partial z} \quad @ \; z = 0 \qquad (4.12\,A)$$

$$\frac{\partial \Pi_{1z}}{\partial z} = \frac{\partial \Pi_{2z}}{\partial z} \quad @ \; z \equiv -d \qquad (4.12\,B)$$

Note that the application of the boundary conditions affects only unknown terms $f_i(\lambda)$. Thus, we can consider these terms independently of their integrals and can write:

at $z = 0$

$$f_0(\lambda) - f_1(\lambda) - f_2(\lambda) = -\lambda/\alpha_0$$

$$f_0(\lambda) + \frac{\alpha_1}{\alpha_0}\left[f_1(\lambda) - f_2(\lambda)\right] = \lambda/\alpha_0 \tag{4.13}$$

and at $z = -d$

$$f_1(\lambda)e^{-\alpha_1 d} + f_2(\lambda)e^{+\alpha_1 d} = f_3(\lambda)e^{-\alpha_2 d}$$

$$\alpha_1\left[f_1(\lambda)e^{-\alpha_1 d} - f_2(\lambda)e^{+\alpha_1 d}\right] = \alpha_2 f_3(\lambda)e^{-\alpha_2 d} \tag{4.14}$$

To determine π_{0z}, the Hertz vector on and above the surface, we need to find $f_0(\lambda)$ in terms of α_1, α_2, and d. Solving (4.13) and (4.14) for $f_0(\lambda)$ we determine that:

$$f_0(\lambda) = \frac{\lambda}{\alpha_0}\left\{\frac{\left(\frac{\alpha_1 - \alpha_2}{\alpha_1 + \alpha_2}\right)e^{-2\alpha_1 d} - \left(\frac{\alpha_1 - \alpha_0}{\alpha_1 + \alpha_0}\right)}{1 - \left(\frac{\alpha_1 - \alpha_0}{\alpha_1 + \alpha_0}\right)\left(\frac{\alpha_1 - \alpha_2}{\alpha_1 + \alpha_2}\right)e^{-2\alpha_1 d}}\right\} \tag{4.15}$$

and

$$\Pi_{0z} = \frac{m}{4\pi}\int_0^\infty\left[\frac{\lambda}{\alpha_0}J_0(\lambda r)e^{-\alpha_0 z}\right]\left[1 + \frac{\left(\frac{\alpha_1 - \alpha_2}{\alpha_1 + \alpha_2}\right)e^{-2\alpha_1 d} - \left(\frac{\alpha_1 - \alpha_0}{\alpha_1 + \alpha_0}\right)}{1 - \left(\frac{\alpha_1 - \alpha_0}{\alpha_1 + \alpha_0}\right)\left(\frac{\alpha_1 - \alpha_2}{\alpha_1 + \alpha_2}\right)e^{-2\alpha_1 d}}\right]d\lambda \tag{4.16}$$

Noting that

$$\alpha_0 = (\lambda^2 - k_0^2)^{\frac{1}{2}} = (\lambda^2 - i\sigma_0\mu_0\omega + \varepsilon_0\mu_0\omega^2)^{\frac{1}{2}}$$

$$= (\lambda^2 + \varepsilon_0\mu_0\omega^2)^{\frac{1}{2}} \qquad (4.17A)$$

and ignoring displacement currents, we can write:

$$\alpha_0 = \lambda \qquad (4.17B)$$

and (4.16) can be written in the form:

$$\Pi_{0z} = \frac{m}{4\pi}\int_0^\infty J_0(\lambda r)e^{-\lambda z}\left[\,|\,+\frac{\left(\frac{\alpha_1-\alpha_2}{\alpha_1+\alpha_2}\right)e^{-2\alpha_1 d}-\left(\frac{\alpha_1-\lambda}{\alpha_1+\lambda}\right)}{|\,-\left(\frac{\alpha_1-\lambda}{\alpha_1+\lambda}\right)\left(\frac{\alpha_1-\alpha_2}{\alpha_1+\alpha_2}\right)e^{-2\alpha_1 d}}\right]d\lambda \qquad (4.18)$$

Using equation (4.5) to find H_z and H_r we find that:

$$H_z = \frac{m}{4\pi}\int_0^\infty \lambda^2 J_0(\lambda r)e^{-\lambda z}\left[\,|\,+\frac{\left(\frac{\alpha_1-\alpha_2}{\alpha_1+\alpha_2}\right)e^{-2\alpha_1 d}-\left(\frac{\alpha_1-\lambda}{\alpha_1+\lambda}\right)}{|\,-\left(\frac{\alpha_1-\lambda}{\alpha_1+\lambda}\right)\left(\frac{\alpha_1-\alpha_2}{\alpha_1+\alpha_2}\right)e^{-2\alpha_1 d}}\right]d\lambda \qquad (4.19)$$

and

$$H_r = \frac{m}{4\pi}\int_0^\infty \lambda^2 J_1(\lambda r)e^{-\lambda z}\left[\,|\,+\frac{\left(\frac{\alpha_1-\alpha_2}{\alpha_1+\alpha_2}\right)e^{-2\alpha_1 d}-\left(\frac{\alpha_1-\lambda}{\alpha_1+\lambda}\right)}{|\,-\left(\frac{\alpha_1-\lambda}{\alpha_1+\lambda}\right)\left(\frac{\alpha_1-\alpha_2}{\alpha_1+\alpha_2}\right)e^{-2\alpha_1 d}}\right]d\lambda \qquad (4.20)$$

Letting $\alpha = \lambda$ in equation 4.7 we note that:

$$\frac{m}{4\pi R} = \frac{m}{4\pi}\int_0^\infty J_0(\lambda r)e^{-\lambda z}\,d\lambda \tag{4.21}$$

and

$$\frac{\partial^2}{\partial z^2}\left(\frac{m}{4\pi R}\right) = \int_0^\infty \lambda^2 J_0(\lambda r)e^{-\lambda z}\,d\lambda \tag{4.22A}$$

$$\frac{\partial^2}{\partial r \partial z}\left(\frac{m}{4\pi R}\right) = \int_0^\infty \lambda^2 J_1(\lambda r)e^{-\lambda z}\,d \tag{4.22B}$$

Thus, we can write equation 4.19 in the form:

$$H_z = \frac{-m}{4\pi R^3} + \frac{3mz^2}{4\pi R^5} + \frac{m}{4\pi}\int_0^\infty \left\{J_0(\lambda r)e^{-\lambda z}\lambda^2\right\} \left\{\frac{(\alpha_1 + \lambda)(\alpha_1 - \alpha_2)e^{-2\alpha_1 d} + (\alpha_1 - \lambda)(\alpha_1 + \alpha_2)}{(\alpha_1 + \lambda)(\alpha_1 + \alpha_2) - (\alpha_1 - \lambda)(\alpha_1 - \alpha_2)e^{-2\alpha_1 d}}\right\} d\lambda \tag{4.23}$$

and equation 4.20 in the form:

$$H_r = \frac{+3mrz}{4\pi R^5} + \frac{m}{4\pi}\int_0^\infty \left\{J_1(\lambda r)e^{-\lambda z}\lambda^2\right\} \left\{\frac{(\alpha_1 + \lambda)(\alpha_1 - \alpha_2)e^{-2\alpha_1 d} - (\alpha_1 - \lambda)(\alpha_1 + \alpha_2)}{(\alpha_1 + \lambda)(\alpha_1 + \alpha_2) - (\alpha_1 - \lambda)(\alpha_1 - \alpha_2)e^{-2\alpha_1 d}}\right\} d\lambda \tag{4.24}$$

Following closely the analysis of Wait (1958), we shall normalize equations (4.23) and (4.24) by dividing these expressions for H_z and H_r by the expression for the primary H_z field (i.e., the first two terms of equation (4.23) and we shall, in addition, put these normalized expressions in forms convenient for numerical integration.

Accordingly, the expression for the normalized magnetic field can be put in the form:

$$H_z^n = \frac{(R/\delta)^3}{1 - 3(z/R)^2} T_0(A,B) + 1 \qquad (4.25)$$

and the expression for the normalized radial magnetic field can be put in the form:

$$H_r^n = \frac{(R/\delta)^3}{1 - 3(z/R)^2} T_1(A,B) - \frac{(3rz)/R^2}{1 - 3(z/R)^2} \qquad (4.26)$$

where:

$$T_i(A,B) = \int_0^\infty R(D,g)\ g^2\ e^{-gA}\ J_i(gB)\ dg \qquad (4.27)$$

where:

J_i is the Bessel function of the first kind of order i, and:

$$R(D,g) = 1 - \frac{2g\left\{U(1 + e^{-UD}) + V(1 - e^{-UD})\right\}}{U(g + V)(1 + e^{-UD}) + (U^2 + gV)(1 - e^{-UD})}$$

$$= 1 - \frac{2g\left\{(U + V) + (U - V)e^{-UD}\right\}}{(U + g)(U + V) - (U - g)(U - V)e^{-UD}} \qquad (4.28)$$

where:

$$U = (g^2 + i2)^{\frac{1}{2}} \tag{4.29A}$$

$$V = (g^2 + i2\,\frac{\sigma_2}{\sigma_1})^{\frac{1}{2}} \tag{4.29B}$$

$$\delta = \left(\frac{2}{\sigma_1 \mu_0 \omega}\right)^{\frac{1}{2}} \approx \frac{503.8}{(\sigma_1 f)^{\frac{1}{2}}} \tag{4.29C}$$

$$A = \frac{z + h}{\delta} \tag{4.29D}$$

$$B = \frac{r}{\delta} \tag{4.29E}$$

$$D = \frac{2\,d}{\delta} \tag{4.29F}$$

$$r^2 = x^2 + y^2 \tag{4.29G}$$

$$R^2 = r^2 + (z - h)^2 \tag{4.29H}$$

It should be noted that for all practical source receiver separations where $z \ll r$, so that $r \approx R$, equations (4.25) and (4.26) reduce to:

$$H_z^n = \left(\frac{r}{\delta}\right)^3 T_0(A,B) + 1 \tag{4.30}$$

and

$$H_r^n = \left(\frac{r}{\delta}\right)^3 T_1(A,B) - \frac{3z}{r} \tag{4.31}$$

4.3 Integral calculation

To evaluate equations (4.25) and (4.26) we have to evaluate the Bessel function integral of (4.27). For this purpose, we follow closely the numerical integration technique developed by Longman (1957).

First, we let:

$$y = gB \tag{4.32}$$

So:

$$T_i(A,B) = \int_0^\infty R\left(D,\frac{y}{B}\right)\left(\frac{y}{B}\right)^2 e^{-\frac{yA}{B}} J_i(y)\, d\left(\frac{y}{B}\right)$$

$$= \frac{1}{B^3}\int_0^\infty R\left(D,\frac{y}{B}\right) y^2 \exp\left[\frac{-y(z+h)}{r}\right] J_i(y)\, dy$$

$$= \frac{1}{B^3}\int_0^\infty F(y)\, J_i(y)\, dy \tag{4.33}$$

where:

$$F(y) = R\left(D, \frac{y}{B}\right) y^2 \exp\left[\frac{-y(z+h)}{r}\right] \tag{4.34}$$

The integrals $T_i(A,B)$ then are evaluated as the sum of a set of integrals, each taken between successive zeros of $J_i(y)$:

$$T_i(A,B) = \frac{1}{B^3}\left\{\int_0^{z_{i,1}} F(y)\ J_i(y)\ dy + \int_{z_{i,1}}^{z_{i,2}} F(y)\ J_i(y)\ dy + \text{---}\right\}$$

$$= \frac{1}{B^3}\left\{\int_0^{z_{i,1}} F(y)\ J_i(y)\ dy + \sum_{j=1}^{\infty} \int_{z_{i,j}}^{z_{i,j+1}} F(y)\ J_i(y)\ dy\right\}$$

$$= \frac{1}{B^3}\left\{S_{i,0}(y) + \sum_{j=1}^{\infty} S_{i,j}(y)\right\} \qquad (4.35)$$

where:

0, $(z_{i,1})$, $(z_{i,2})$--- are the successive values of y for which $J_i(y)$ is zero

and:

$$S_{i,0}(y) = \int_0^{z_{i,1}} F(y)\ J_i(y)\ dy \qquad (4.36A)$$

$$S_{i,j}(y) = \int_{z_{i,j}}^{z_{i,j+1}} F(y)\ J_i(y)\ dy \qquad (4.36B)$$

To evaluate the integrals $S_{i,j}(y)$ we use the 16 point Gaussian quadrature approximation:

$$\int_{-1}^{1} f(X)\, dX = \sum_{k=1}^{16} W_k\, f(X_k) + Rm \qquad (4.37A)$$

or, transforming the limits:

$$\int_{P}^{Q} f(X)\, dX = \frac{Q-P}{2} \sum_{k=1}^{16} W_k\, f\left(\frac{Q-P}{2} X_k + \frac{Q+P}{2}\right) + Rm \qquad (4.37B)$$

where W_k and X_k are the Gaussian values listed in Table 4-1.

So:

$$S_{i,j}(y) = \frac{z_{i,j+1} - z_{i,j}}{2} \sum_{k=1}^{16} W_k\, F(y_{i,j,k})\, J_i(y_{i,j,k}) + Rm$$

$$= \sum_{k=1}^{16} C_{i,j,k}\, F(y_{i,j,k}) + Rm \qquad (4.38)$$

where:

$$C_{i,j,k} = \frac{z_{i,j+1} - z_{i,j}}{2} W_k\, J_i(y_{i,j,k}) \qquad (4.39A)$$

$$y_{i,j,k} = \frac{z_{i,j+1} - z_{i,j}}{2} X_k + \frac{z_{i,j+1} - z_{i,j}}{2} \qquad (4.39B)$$

Table 4-1

Gaussian Integration Coefficients (W_k) and Abcissas (X_k)

X_k	W_k
-0.989400934991650	0.027152459411754
-0.944575023073233	0.062253523938648
-0.865631202387832	0.095158511682493
-0.755404408355003	0.124628971255534
-0.617876244402644	0.149595988816577
-0.458016777657227	0.169156519395002
-0.281603550779259	0.182603415044924
-0.095012509837637	0.189450610455068
0.095012509837637	0.189450610455068
0.281603550779259	0.182603415044924
0.458016777657227	0.169156519395002
0.617876244402644	0.149595988816577
0.755404408355003	0.124628971255534
0.865631202387832	0.095158511682493
0.944575023073233	0.062253523938648
0.989400934991650	0.027152459411754

We evaluated the expressions for the normalized magnetic field (equations 4.25 and 4.26) on an IBM S/370 Model 165 computer using double precision arithmetic to evaluate the terms $T_i(A,B)$. This degree of precision (16 decimal digits) was found to be necessary to avoid roundoff errors because the evaluation hinged on small differences between large numbers; in retrospect, we realized that this problem could have been minimized by rephrasing the equations in terms of a halfspace solution and perturbations thereon. The integrals $S_{i,j}(y)$ (equation 4.38) were summed over the first 100 zeros of the Bessel functions $J_i(y)$ and a one term Euler transformation was performed on the summation by subtracting half of the last term, $S_{i,100}(y)$. We determined early in the process that this brute force approach would yield more than adequate rigor for our purpose and, because of the pressure of time, we did not investigate the reduction in computer running time that we realized could have been achieved by reducing the number of zeros and using more terms in the Euler transformation. The term $(1 - e^{-UD})$ was set equal to unity for values of UD greater than 39, because for this value $\mathrm{Re}|e^{-UD}| \leq 10^{-16}$ and, since the computer carries a double precision variable as a 16 decimal digit number, values beyond this limit simply cause an underflow to occur without contributing anything useful to the results.

4.4 Review

In this chapter, we have derived expressions for the near surface normalized magnetic fields produced by a small current loop deployed on the surface of a layered conducting earth, and described the numerical integration techniques which we employed to evaluate the resulting expressions.

In the next chapter, we describe field measurements made at two test sites near El Paso, Texas. Chapter 6 then provides an analysis of these field measurements based on the preceding theoretical formulations.

It should be noted that our data analysis to date has concentrated on a two layer theoretical formulation which proved adequate for the immediate purpose. As opportunity arises in the future we would expect to incorporate into our computer program the multilayer analysis and inversion techniques explained in the appendices.

5.0 A Field Trial

A field trial was conducted near El Paso, Texas, during the month of October, 1973. This field trial was intended to be a rapid test of the concept and feasibility of the low frequency inductive technique for geophysical prospecting. For this reason, no attempt was made to refine the final hardware, but, rather, a collection of immediately available "black boxes" was assembled into a system with the sole criterion that the electrical performance had to be adequate to permit a realistic feasibility test.

The El Paso area was selected for the initial field trial for several reasons. First, this area is quite arid and representative of areas where there is a real need for subsurface water prospecting techniques. Second, the area has been studied extensively in the past so that a comparative data base exists. Third, specific areas of interest are readily accessible. Fourth, and importantly, because the entire region relies on subsurface water, there are a very large number of operating wells that provide positive assurance of the depth and quality of the subsurface water.

The climate is shown in Figure 5-1. The average annual rainfall in the area is only seven inches, a figure that is comparable with the rainfall in many areas of West Africa. The groundwater in the area has been described by Leggat, Lowry, and Hood (1963). Although we used their study as general background information, the depths to water, as well as current conditions, were provided by Walter Meyer of the U.S. Geological Survey at the El Paso office. Additional geophysical data were available from Zhody (1969).

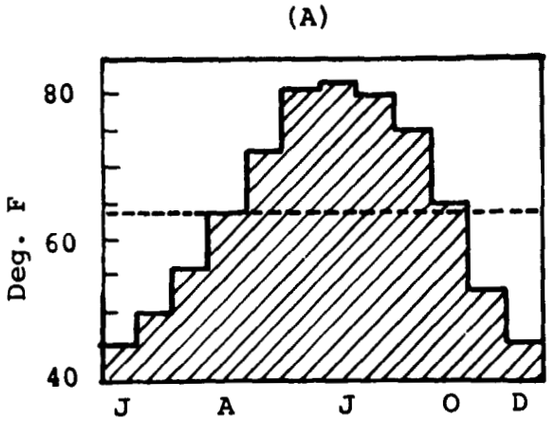

Average monthly temperature at El Paso, Texas

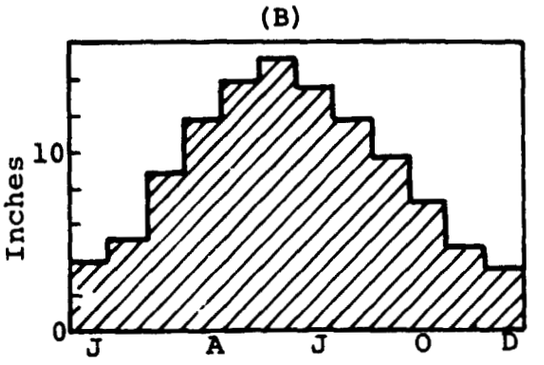

Average monthly evaporation at Ysleta, Texas

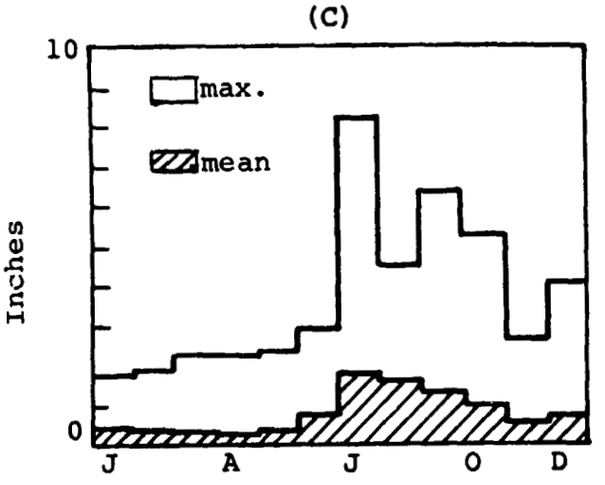

Precipitation range by month at El Paso, Texas

Figure 5-1. Climate in vicinity of El Paso, Texas, 1878-1958. (From U.S. Weather Bureau records. After Leggat et al, 1963.)

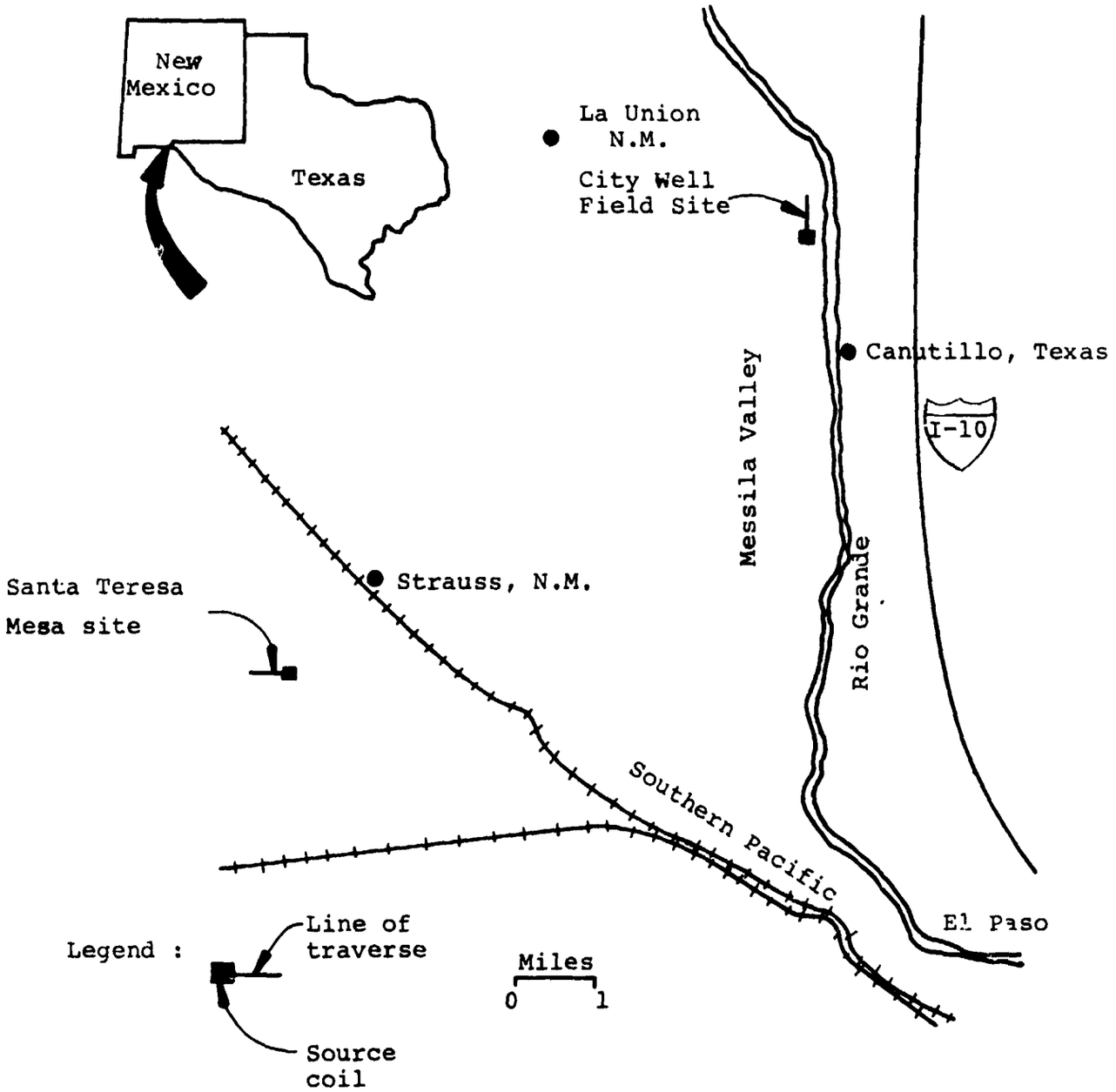

Figure 5-2. Map Showing Sites near El Paso, Texas

In Figure 5-2 we show the location of the two sites that were used: in the Messila Valley at the City Well Field and on the Santa Teresa Mesa. These locations were chosen because they offered good calibration of depths to water on the basis of numerous wells, and because they offered markedly different depths to the water table. The site used in the Messila Valley had a depth to the subsurface water of 8.6 meters (28 feet), and the Santa Teresa Mesa site had a subsurface water depth of 100 meters (327 feet).

For the October field trial, the 'source' coil consisted of 12 turns of #10 wire laid on the ground in a square with a side of 25 meters, and energized with currents ranging from 15 amperes at 60 hertz to 5 milliamperes at 20 kilohertz. The 'detector' coil consisted of 1200 turns of #26 wire wound on a one meter square wooden supporting structure that could be oriented in either a horizontal or vertical position. The magnitude and phase of the observed signal was measured by means of a commercial phase-locked-loop synchronous detector using a reference signal coupled from the source to the detector by a shielded, twisted pair, cable.

At both sites, data were collected with source-detector separations ranging from 20 to 500 meters. A photograph of the apparatus is shown as Figure 5-3.

Figure 5-4 shows the source energizing equipment which included three motor driven alternators and an oscillator-amplifier combination mounted in a pickup truck. One 3.5 kVA gasoline driven alternator served as a portable power supply for other equipment and also provided a current of 15 amperes at a frequency of 60 hertz that was coupled directly to the source coil. A second, 1.2 kVA, gasoline driven alternator provided a current of

3.1 amperes at a frequency of 400 hertz that was coupled directly to the source coil, and a third gasoline driven alternator provided a current of 1.2 amperes at a frequency of 800 hertz that was similarly coupled directly to the source coil. Other frequencies of 1, 2.5, 7, 16, and 20 kilohertz were derived by using an oscillator to provide input to a high power commercial audio amplifier; currents supplied to the source coil ranged from 800 milliamperes at 1 kilohertz to 5 milliamperes at 20 kilohertz.

The detecting apparatus is shown as Figure 5-5. A wooden framework supported a coil consisting of 1200 turns of #26 wire wound in four separated layers of 300 turns each on a square wooden form with a maximum cross-sectional area of one square meter. The coil structure was mounted on pivots so that it could be oriented in either a horizontal or a vertical plane; final adjustment was accomplished with the aid of levelling bubbles. At the higher frequencies, data were measured using only the inside layer of 300 turns; this layer had a self resonant frequency of 35 kilohertz and a Q of 37. At ranges greater than 300 meters, where the higher frequencies were no longer of interest (because the signal level was too low for measurements), measurements were made only at frequencies of 1000 hertz or less: in this regime we used the full 1200 turns which had a self resonant frequency of 6 kilohertz and a Q of 17. The battery operated synchronous detector was mounted on the framework, in a position chosen to be symmetrical with respect to the coil, and a phase reference signal was provided by a shielded, twisted pair, cable extended between the source and the detector apparatus.

Figure 5-3. Photograph of apparatus used in field trial. The source energizing equipment was mounted in the tarpaulin shaded, pickup truck. Part of the horizontal source coil can be seen in the foreground, and the detector apparatus can be seen in the midground beyond the hood of the pickup truck.

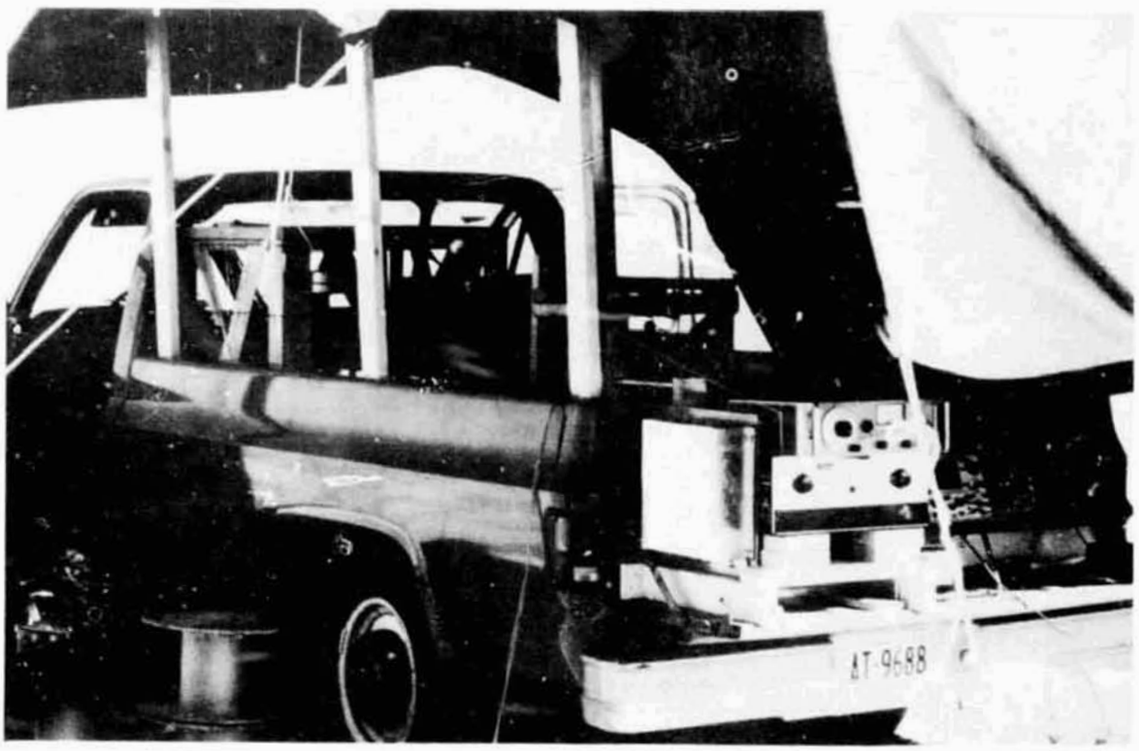

Figure 5-4. Photograph of source energizing equipment. Three alternators (60, 400, and 800 Hertz) were carried in the truck with an oscillator, power amplifier, oscilloscope and switching box mounted on the tailgate.

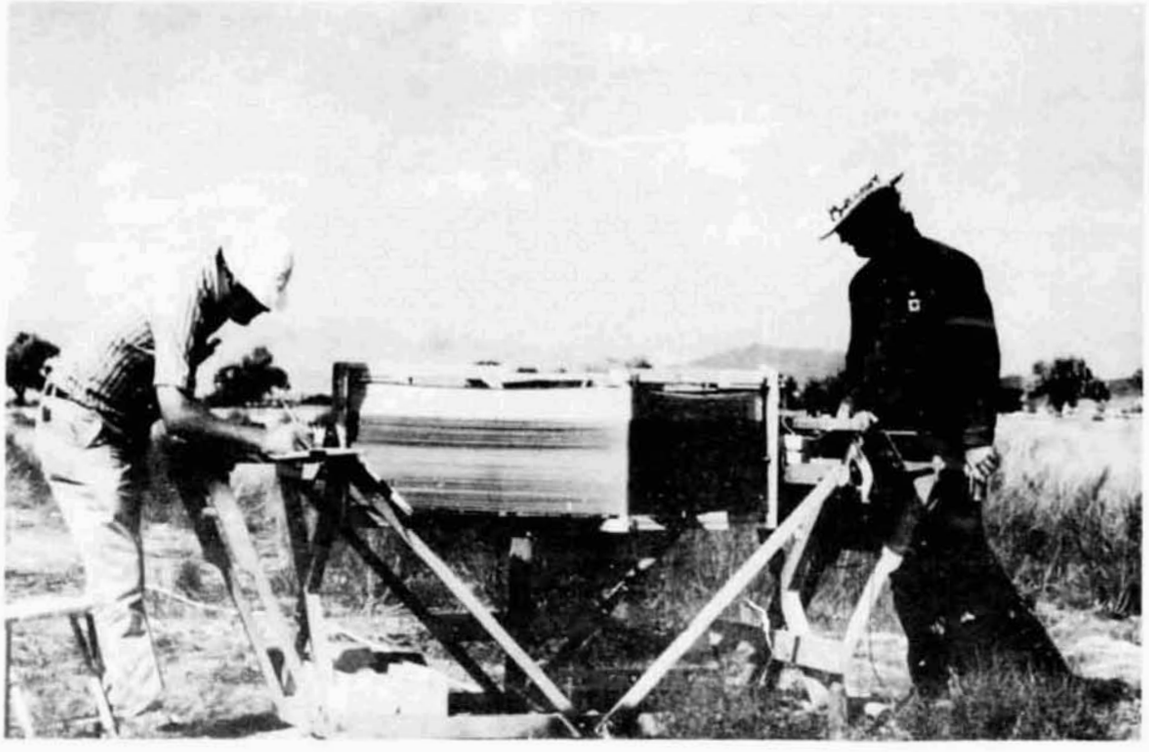

Figure 5-5. Photograph of detector apparatus. 1200 turns of #26 wire were wound on a wooden form that could be rotated to either a vertical or horizontal position. The phase sensitive detector was mounted symmetrically with respect to the coil. A phase reference was provided by a shielded, twisted pair, cable extending from the source apparatus. Small hydraulic jacks were used to level the apparatus at each recording station.

Measurements were made at logarithmically spaced stations ($10^{1.3}$, $10^{1.4}$, $10^{1.5}$, ...) from 20 meters ($10^{1.3}$) to 501 meters ($10^{2.7}$) as the detector apparatus was carried in a straight line away from the source. At each station the magnitude and phase of the voltage existing at the terminals of the coil were recorded, first with the coil vertical and then with the coil horizontal.

Six frequencies were used at each of the shorter range stations but as the range increased the signal-to-noise ratios of the higher frequencies progressively decreased below a useable level. Accordingly, the number of frequencies was reduced until, at the longer ranges, data were recorded only at 60 and 400 hertz. However, since most of the information at long ranges is related to deep layers and can be gleaned from the low frequency data, the absence of higher frequency data at the longer ranges was not detrimental to the feasibility test.

It should be noted that the purpose of the field trial was to test the concept and feasibility of the technique for geophysical probing. The apparatus only vaguely (if at all) resembled a final operational system. We needed about three hours to deploy and recover the source coil; while the detector apparatus, which weighed more than 100 pounds, had to be manhandled with considerable difficulty. During this field trial, one data run consisting of fifteen stations ranging from 20 to 500 meters from the source occupied two full days of effort with an average time of 16 minutes for each elementary datum point (one frequency at one station). In an operational system, of course, smaller and more efficient source and detector coils would be mounted permanently on vehicles capable of traversing the type of terrain of likely interest. With proper instrumentation of this type we expect to obtain a complete data run in one hour.

6.0 Data Analysis

For our feasibility trial field measurements near El Paso, Texas, we chose sites of known geology. Specifically, we chose sites where the depths to the water table were defined clearly by existing wells, and where we could work over large, apparently homogeneous, areas which appeared to be uniform in all directions from the source coil. Thus, in the data analysis we could fairly assume negligible lateral variations in conductivity, i.e., $\sigma(r,z) \approx \sigma(z)$.

Although we realize that variations in conductivity with depth are rarely abrupt in the type of soils of interest in this investigation, we chose to assume in the data analysis that the subsurface of the test sites consisted of discrete, homogeneous, layers of varying conductivities. That is, we chose to assume in the data analysis that the conductivity with depth could be approximated adequately as a discretely varying parameter, $\sigma(z) = \sigma_i(z)$ where i is the layer number. This assumption of a layered medium greatly simplifies the theoretical problem, allowing us to use the analysis of Chapter 4 and Appendix A for the calculation of the fields induced by an oscillating magnetic dipole near a multi-layered conducting earth.

We assumed in our theoretical models that the permeability of the subsurface was the same as that of free space, μ_0, since the permeability of moist rocks and soils is very close to that of free space except when large quantities of ferrous minerals are present. And, finally, we assumed that displacement currents could be ignored for our low source frequencies. A summary of the above assumptions is listed in Chapter 4.

6.1 Data Quality and Format

During our field tests, we obtained measures of the absolute magnitude and phase (with respect to the phase of the source) of the radial and vertical components of the magnetic field, H_r and H_z, for the frequencies and ranges described in Chapter 5. At each frequency we took data at increasing separations until limited by noise in the receiver. Data points at the maximum range for each frequency, therefore, can be considered to be of suspect quality because they were derived from measurements made with a very low signal-to-noise ratio.

In our analysis we matched theoretical curves derived from expressions for the normalized field components (see Chapter 4) with plots of the measured values. The quantity actually measured in the field is the voltage induced in the receiving loop when the source loop is energized.

For ranges much greater than the height of the receiving coil (the usual situation of interest) the measured voltage is related to the normalized components of the magnetic field by the equation:

$$\begin{pmatrix} E_r^m \\ E_z^m \end{pmatrix} = \frac{i\omega\mu_0 I N_1 A_1 N_2 A_2}{4\pi r^3} \begin{pmatrix} h_r^m \\ h_z^m \end{pmatrix} \qquad (6.1)$$

where $i = (-1)^{1/2}$

ω = source frequency in radians/sec.

μ_0 = permeability of free space = $4\pi \times 10^{-7}$

I = magnitude of source current in amperes

N_1 = number of turns of source loop

A_1 = area of source loop in meters^2

N_2 = number of turns of receiving loop

A_2 = area of receiving loop in meters^2

$\begin{pmatrix} h_r \\ h_z \end{pmatrix}$ = normalized component of the magnetic field in amperes/meter

r = separation of source and receiver in meters.

Normalization of the data, therefore, is achieved by multiplying the measured voltages by the factor:

$$\left(\frac{4\pi r^3}{i\omega\mu_0 I N_1 A_1 N_2 A_2} \right)$$

We should note here that, for convenience in the field trials, we arbitrarily chose the orientation of the receiving loops and the terminal connections so that all phase measurements approached zero degree at short ranges. Accordingly, for consistency in comparing the data with the corresponding theoretical expressions we shifted the phase of the theoretical expression for the radial magnetic field component by 180 degrees; this is simply equivalent to rotating the vertical receiving loop by 180° or reversing the terminal connections to the loop.

6.2 Analytical Development

Initially, we based our analysis on the approximation that the subsurface of the test sites could be considered as consisting of only two layers of different conductivities, with the second layer extending to depths below the detection capability of our apparatus. As we shall show, this approximation proved adequate for the City Well Field site which had a water table at a depth of 9 meters, but inadequate for the Santa Teresa Mesa site which had a water table at 100 meters; for this latter site, we were forced to a three layer model. Time and budget considerations prevented us from extending the theory and the computer programs to the multilayer case in the manner described in the appendices. Instead, we chose to handle the analysis of the Santa Teresa Mesa data by using two different two-layer models in different frequency regimes, one model defined by the first and second layers, and one defined by the second and third layers. It might be noted here that the possibility of separating the problem into two (or more) parts in this manner is one of the attractive features of the inductive coupling technique.

We started the analysis using the simple image theory outlined in Appendix D as the basis of our calculations of the normalized field components H_r and H_z but it soon became evident that the image concept could be applied accurately only at ranges large with respect to the effective skin depth of the upper layers (see Appendix D) and that this restriction limited the usefulness of this approach.

We turned then to the integral solution described in Chapter 4, in order to provide more accurate theoretical curves. The integral solution, indeed, provided a far more accurate description of the data than did the image solution, especially for separations less than the effective skin depth of the upper layers.

However, after laborious attempts to match theoretical curves with data, we found that we still could not achieve plausible fits, and at that point we reexamined the subject of the field measurements and normalization. We determined eventually that our initial analysis problems were due largely to:

a) bias in the measured phase due to a phase error in the reference signal;

b) phase and amplitude errors in the field measurements caused by operating at frequencies too close to the resonant frequency of the receiving coil;

c) errors in the normalization process of converting raw data into a convenient form for analysis, due primarily to an imprecise measurement of the source energizing current and the areas of the loops;

and d) near field errors due to the finite size of the source loop.

All of these problems, save possibly d), were circumvented by simply taking ratios of the magnitudes of the vertical and horizontal field components and differences between their individual phase measurements. By considering ratios of the magnitudes of the field components, most of the errors in the normalization process disappear and only errors in the actual knowledge of range, and short term variations in the amplitude of the source energizing current, remain to hamper matching the theoretical and data curves. Additionally, the effects of receiver loop tuning, if only a function of frequency (not position), disappear. Finally, by considering phase differences $(\phi_z - \phi_r)$, errors due to phase shifts in the reference signal are eliminated, since we can write the measured phases in terms of the real phase plus a bias error which is the same in both the radial (ϕ_r) and vertical (ϕ_z) phase measurements.

Thus, our final choice of data format is bilogarithmic plots of the magnitude ratio $|H_z/H_r|$ versus separation for a discrete set of frequencies, and semilogarithmic plots of the phase difference $(\phi_z - \phi_r)$ versus separation for a discrete set of frequencies. Only near field errors have been neglected in the analysis but these errors occur only at combinations of short ranges and low frequencies where little useful information can be inferred from the data.

Before presenting the results of our analysis, we shall first present the technique we ultimately used to determine the nature and bounds of the variation of conductivity with depth so that we could judiciously choose an initial conductivity model for the El Paso field sites.

6.3 An Initial Interpretation Scheme

One method of presenting the data in a form diagnostic of conductivity variations with depth is to plot, on a bilogarithmic scale, the magnitude of the ratio H_z/H_r versus the quantity:

$$(r^2 \pi \mu_0 f)^{1/2} = \left(\frac{r}{\delta_{eff}}\right) \sigma_{eff}^{1/2}$$

For, if the earth could be considered as a homogeneous half space characterized by a single conductivity σ, then $\sigma_{eff}=\sigma$ and plots of data, for various source-receiver separations (r) and frequencies (f_i), would fall on a single curve. Conversely, if the conductivity were a function of depth, plots of the data at each range for a fixed set of frequencies would tend to fall on separate curves, the shapes and positions of which would be dependent on the nature of the conductivity variations. For example, if the conductivity increased monotonically as a function of depth, σ_{eff} would increase with increasing r for a fixed set of frequencies and, correspondingly, the curves would be translated to the left for increasing values of r. Conversely, monotonically decreasing values of conductivity with depth would result in the ratio curves being translated to the right with increasing values of separation r.

For the two layer case where the upper layer is less conductive than the lower layer, the ratio data curves, therefore, will tend to merge, as the separation is increased, on a single curve characteristic of a half space whose conductivity is that of the lower layer; whereas, as the separation is decreased, the ratio data curves will tend to merge with a half space curve

characterized by the conductivity of the upper layer.

For the multilayered case, multiple half space asymptotes will occur from which an estimate of the vertical conductivity profile can be determined.

We realize that an analogous technique could be used to derive an initial interpretation based on the phase data; however, time and budget considerations prevented us from pursuing this possibility.

We conducted our analysis, therefore, by making an initial assessment of the vertical conductivity profile based on magnitude ratio alone, and we then obtained a final corroboration of the interpretation by comparing the data curves for both magnitude and phase with model curves generated on the basis of these initial estimates.

6.4 City Well Field Results

Applying the inspection technique outlined in the preceding section, we can infer that the average value of conductivity tends to increase with depth (Figures 6-1 and 6-2). We note in the Well Field data that the ratio curves tend to merge on a single curve for ranges greater than 150 meters to the maximum range of 501 meters. By matching a half space model curve to the data for ranges greater than 150 meters, we can readily infer a conductivity[1] of 0.1 siemens/meter. Thus, we can assume that a fairly thick layer of 0.1 siemens/meter must exist at a depth less than 150 meters. As range is decreased below 150 meters, each subsequent data curve tends to move closer toward a single curve representing a conductivity of the order of 0.01 siemens/meter. Additionally, we can deduce that the thickness of the upper layer must be less than 25 meters since the data curves have not merged on a single curve for ranges as small as 25 meters and the presence of the lower layer is still noticed in the data.

To arrive at our final model of conductivity as a function of depth, we then plotted two layer theoretical model curves in the forms of magnitude ratio $|H_z/H_r|$ versus separation on a bilogarithmic scale and phase difference $(\phi_z - \phi_r)$ versus separation (r) on a semi-logarithmic scale. We chose model parameters consistent with the asymptotic behavior of the data curves, as described in the previous paragraph, and compared our theoretical models with the data plotted in the same forms.

(1) The term "siemens" and the symbol "S" have been adopted for the unit of conductance previously referred to as the "mho". Use of this term has been approved by the IEEE, IEC, ISO, and Conference Generale des Poids et Mesures.

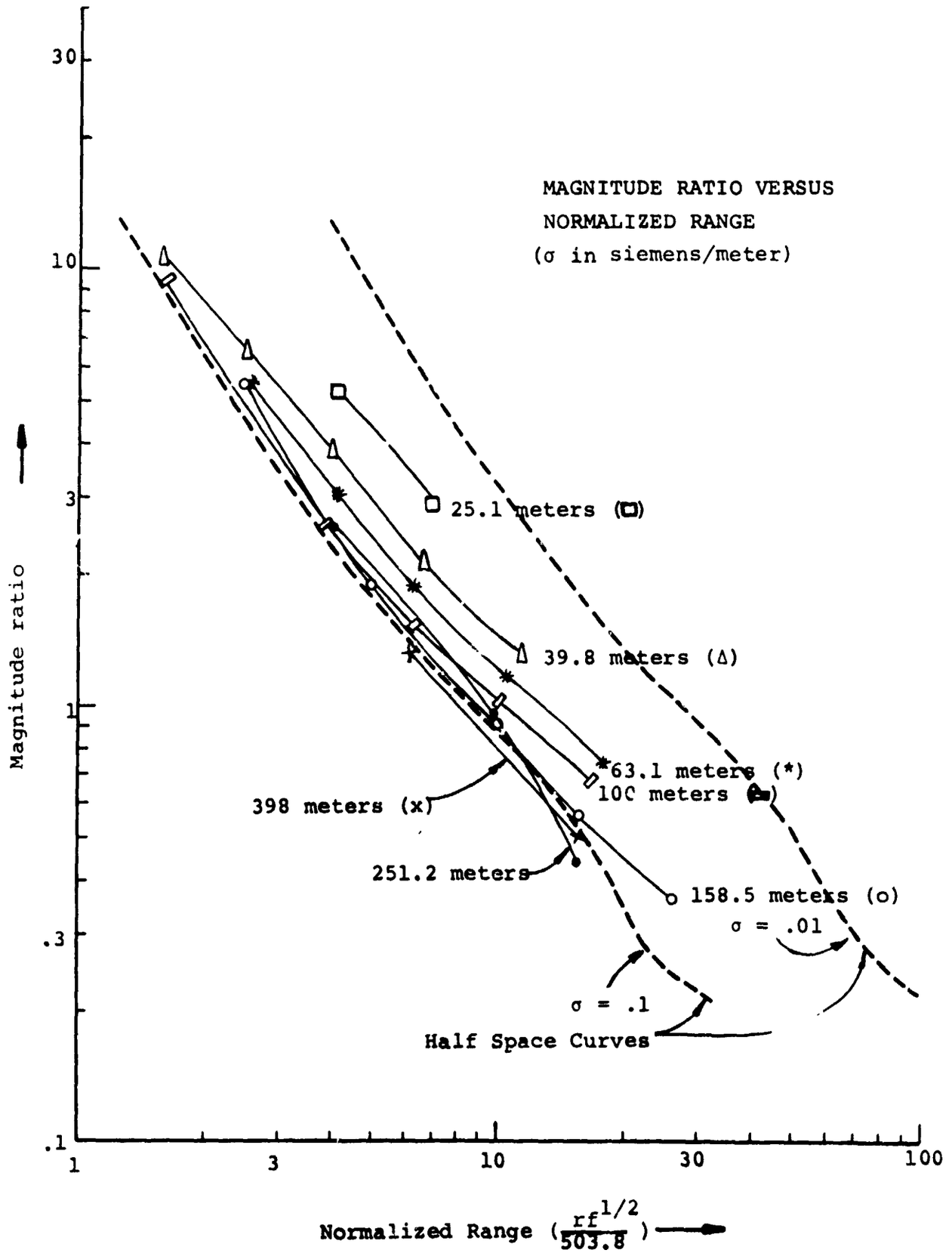

Figure 6-1. City Well Field Data - I

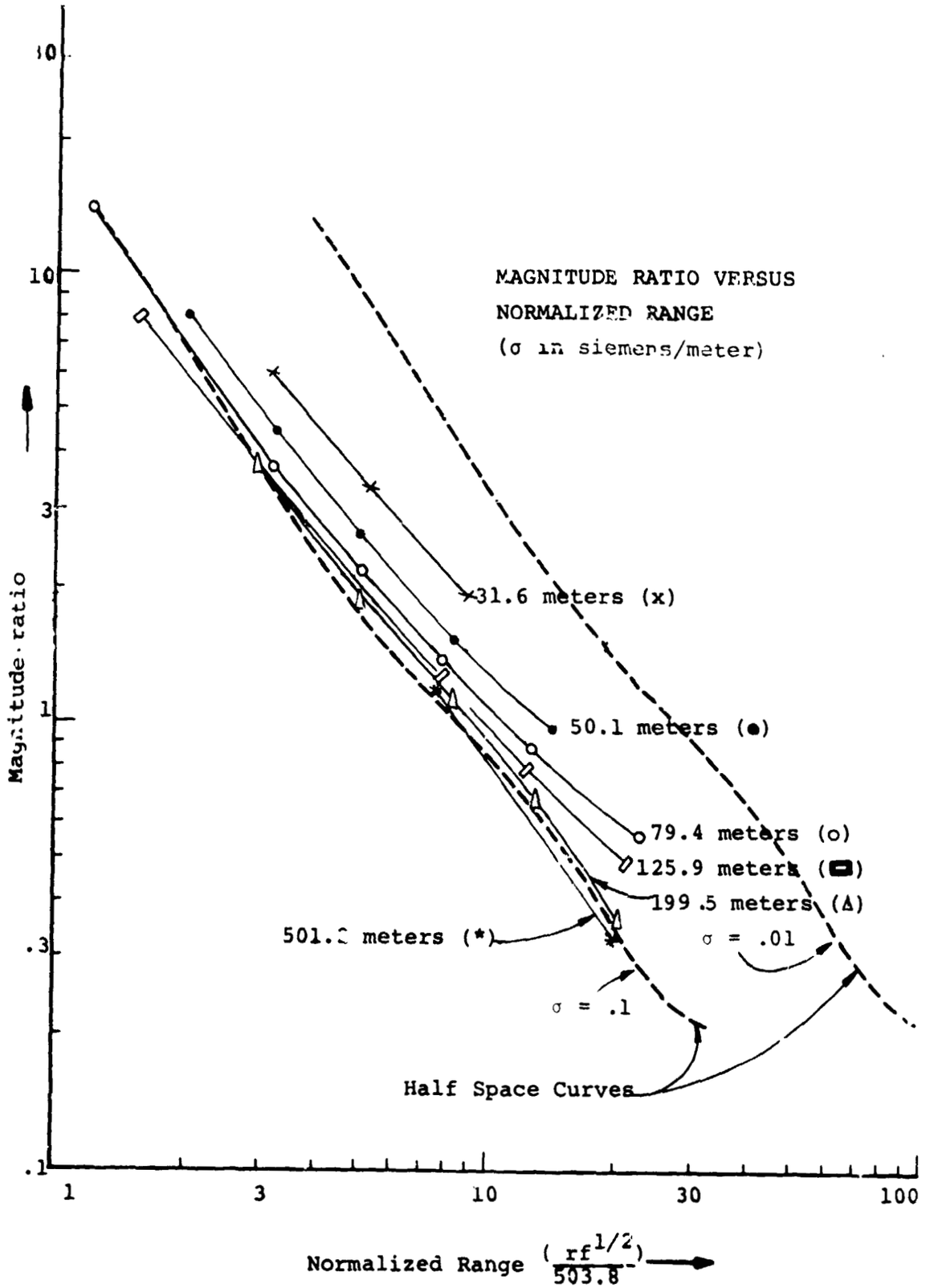

Figure 6-2. City Well Field Data - II

After performing several parameter iterations, we deduced the two layer model illustrated in Figure 6-3a though we realized that the upper layer conductivity of 0.01 siemens/meter is only an average value for the upper 9 meters and that the conductivity of the upper few meters is a much lower value.

The curve matches on which this model is based are presented as Figures 6-4 through 6-9, and as we can see in the high frequency curve matches (6-8 and 6-9), the best fits occur for a marked gradation in conductivity for the upper nine meters. (Note that 6-8 and 6-9 use depths of 6 and 4 meters for the upper layer.) Our interpretation of this vertical conductivity profile is that the rapid increase in conductivity in the upper nine meters is due to an increase in moisture with depth terminating in the water table at nine meters where no further increases in conductivity are detected. We also infer from the high level of conductivity below nine meters (0.1 siemens/meter), that the water tends to be brackish.

For comparison with our interpretation of the City Well Field site, we present as Figure 6-3b a smoothed set of well log resistivity measurements taken near our test site and supplied by Walt Meyer of the U.S.G.S. in El Paso, Texas.

Clearly our model is consistent with the depth to the water table and the average value of conductivity of the layer of soil directly above the water table. Our assessment of the conductivity of the lower water saturated layer appears consistent with the well log to approximately 70 meters beyond which the U.S.G.S. data indicates that the conductivity tends to decrease with further increases in depth. Thus, we must conclude that we could not detect the decrease in conductivity with the

frequencies and separations we used for depth sounding the City Well Field site. Wait and Fuller (1972) have described analytically this limitation inherent in the induction sounding technique when attempting to detect deep resistive layers overlain by more conductive layers. However, although we were unable with our feasibility test instrumentation to detect the presence of the resistive zone below 70 meters, we were able to detect the conductivity contrast attributable to the presence of ground water.

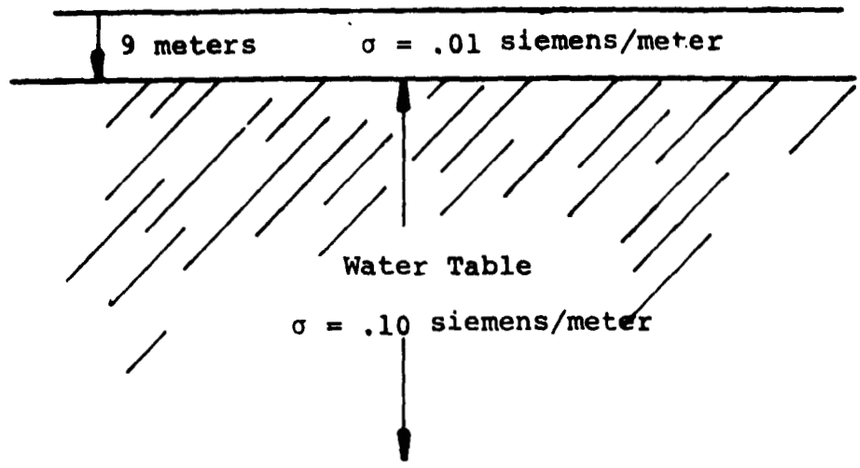

Figure 6-3(a). Interpreted Vertical Conductivity Profile for the City Well Field Test Site.

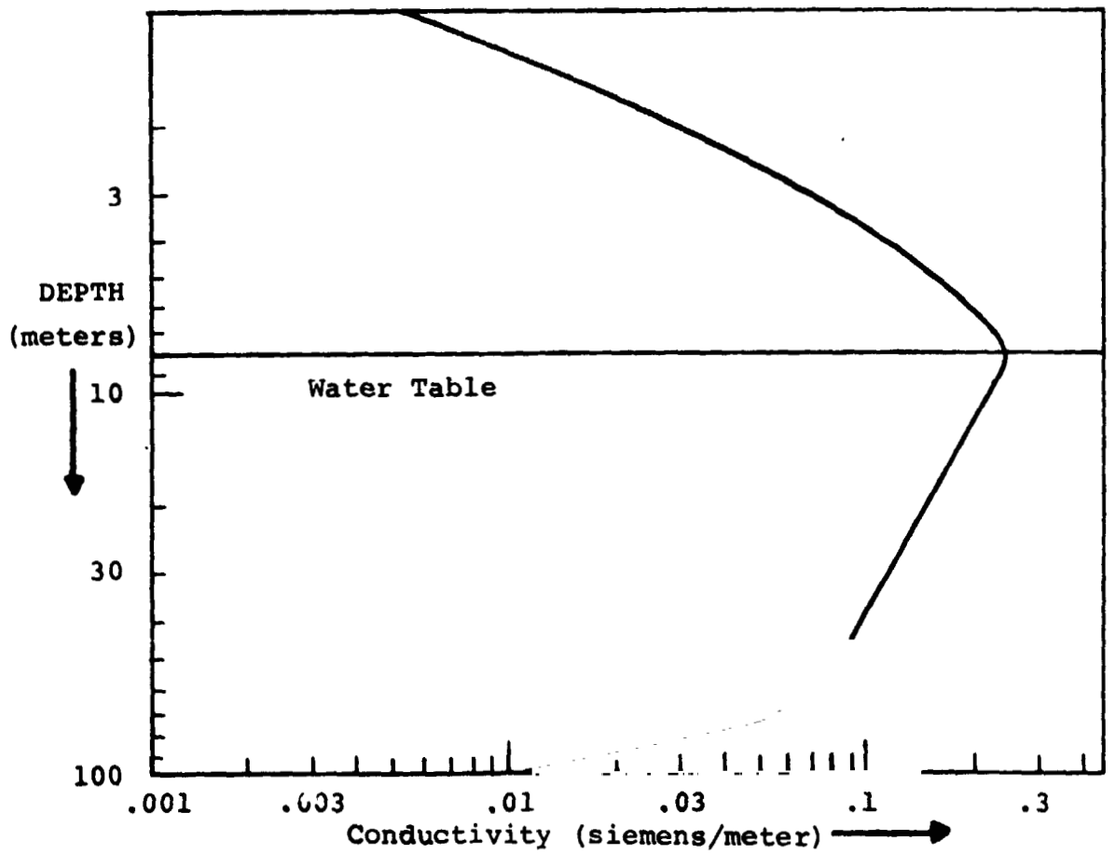

Figure 6-3(b). Reconstruction of U.S.G.S. Well Log Resistivity Data from Nearby City Well.

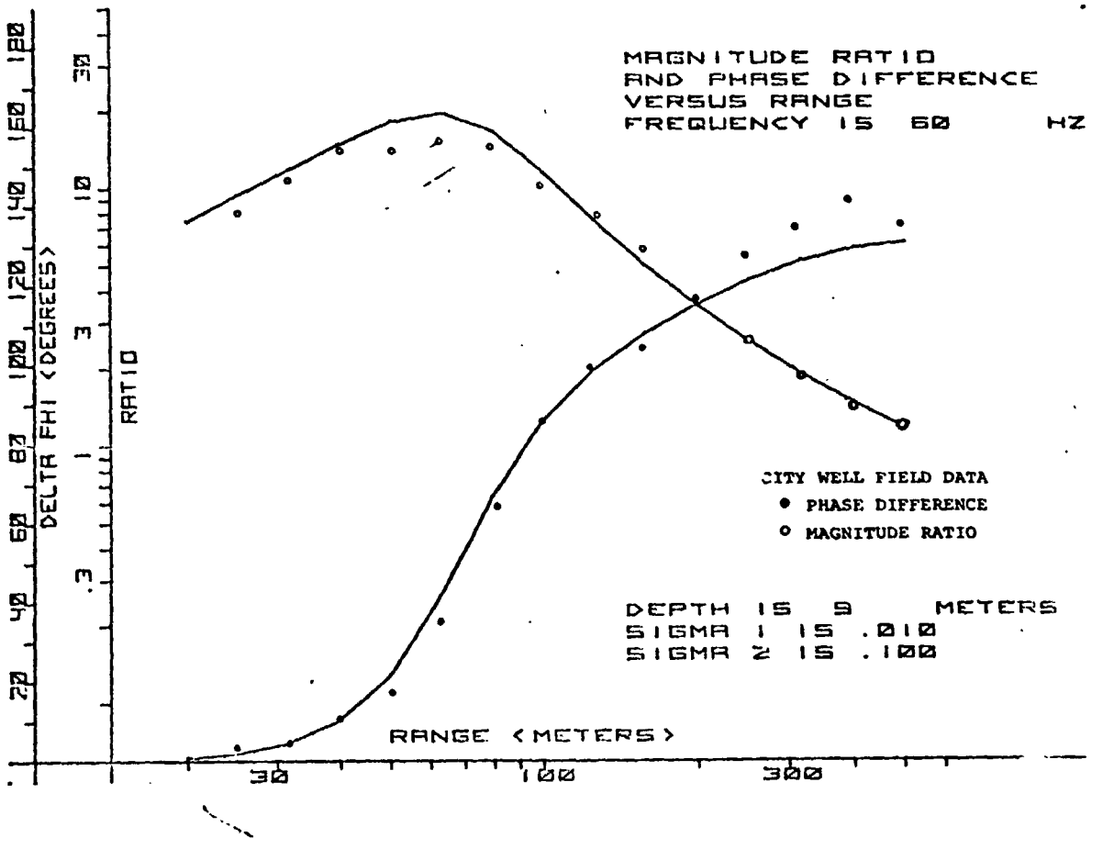

Figure 6-4. Model Curves Compared with City Well Field Data: 60 Hertz

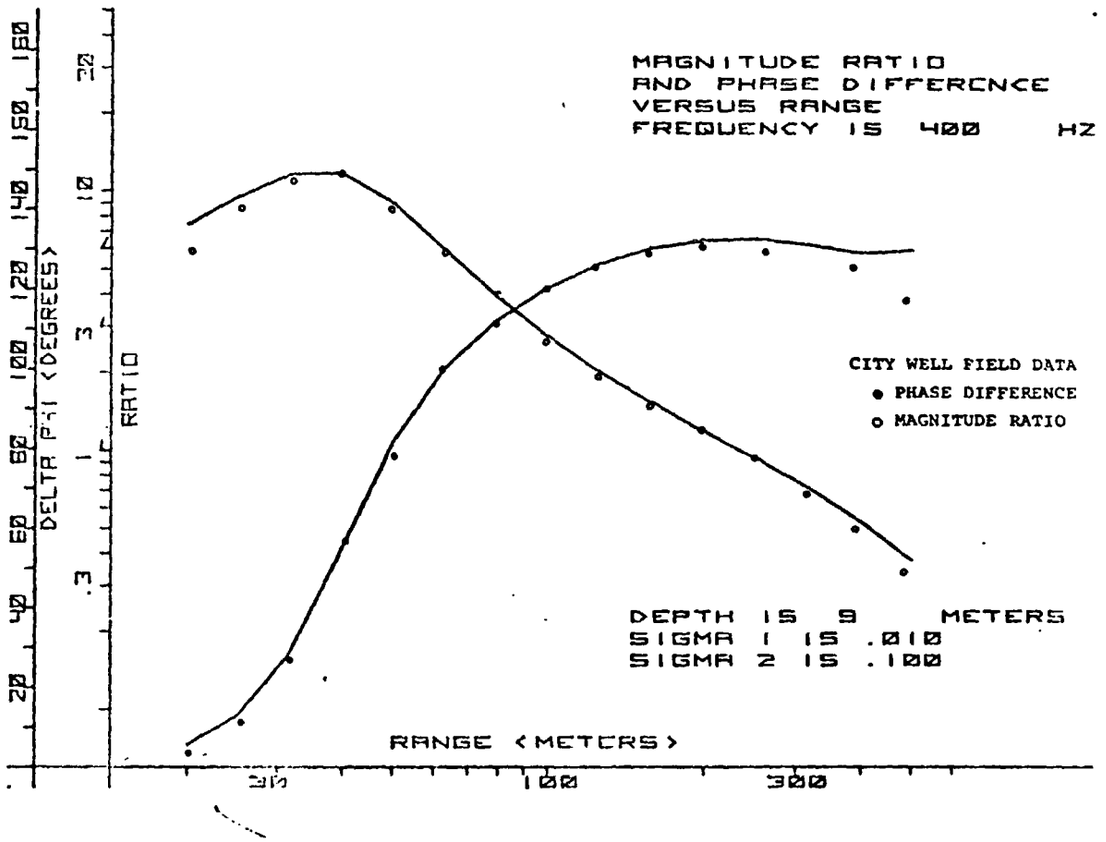

Figure 6-5. Model Curves Compared with City Well Field Data: 400 Hertz.

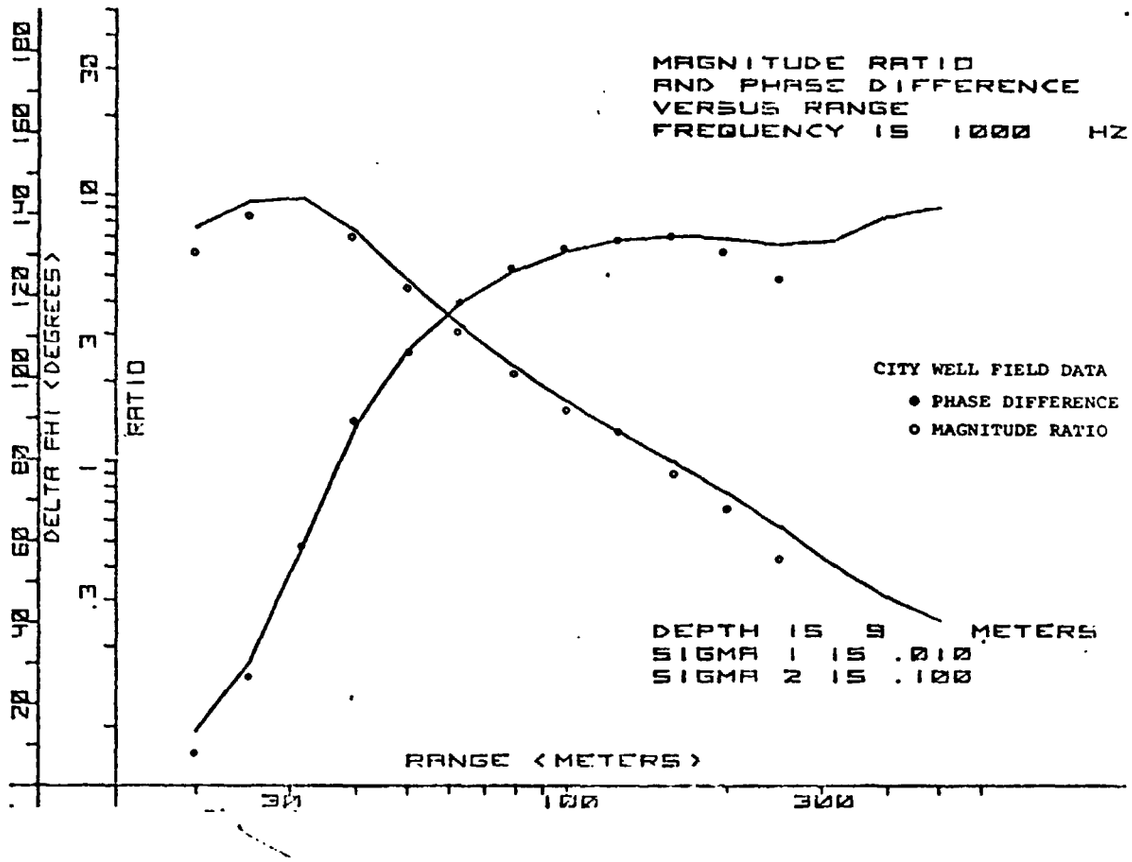

Figure 6-6. Model Curves Compared with City Well Field Data: 1000 Hertz.

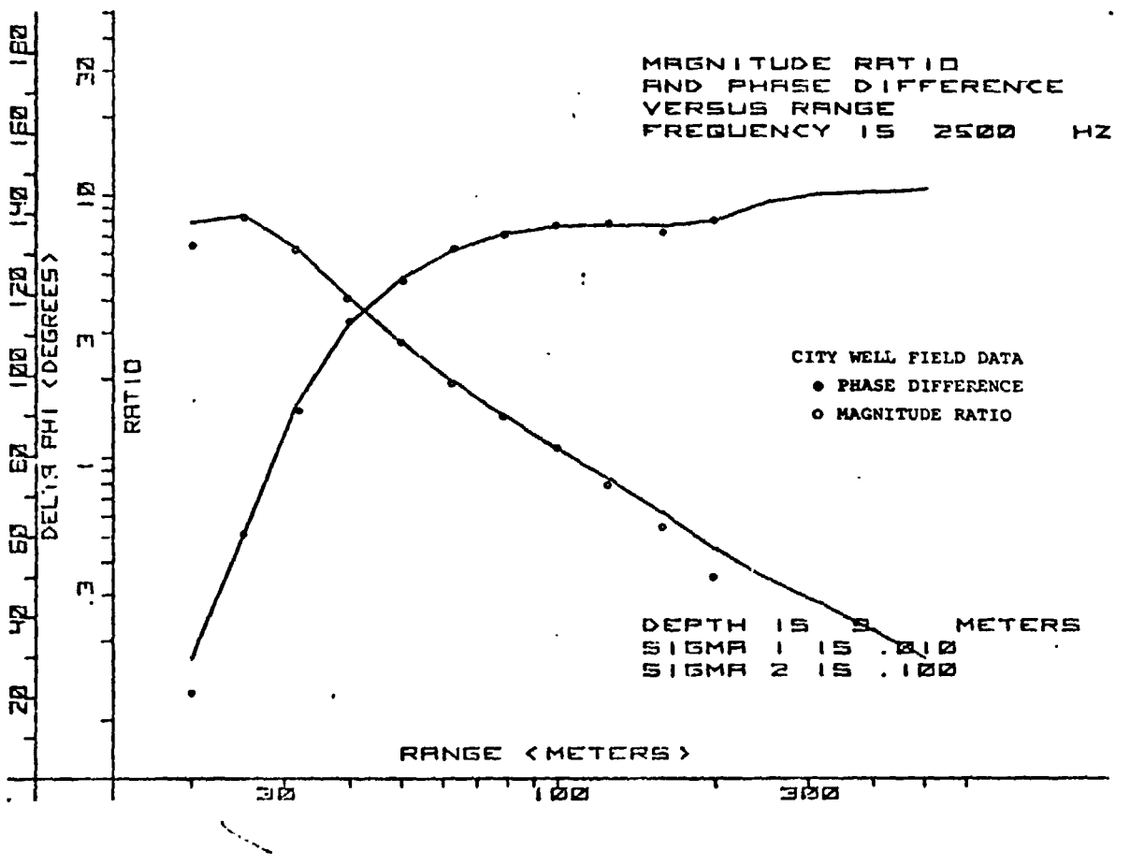

Figure 6-7. Model Curves Compared with City Well Field Data: 2500 Hertz.

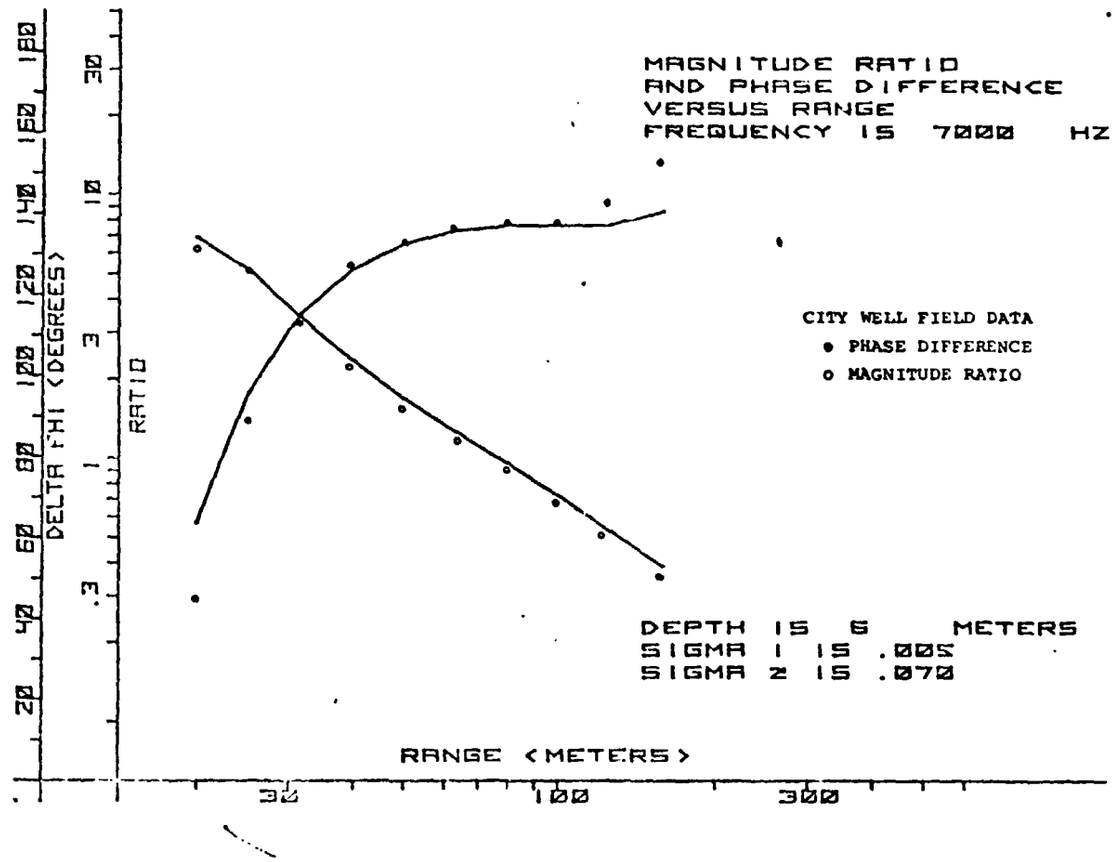

Figure 6-8. Model Curves Compared with City Well Field Data: 7000 Hertz.

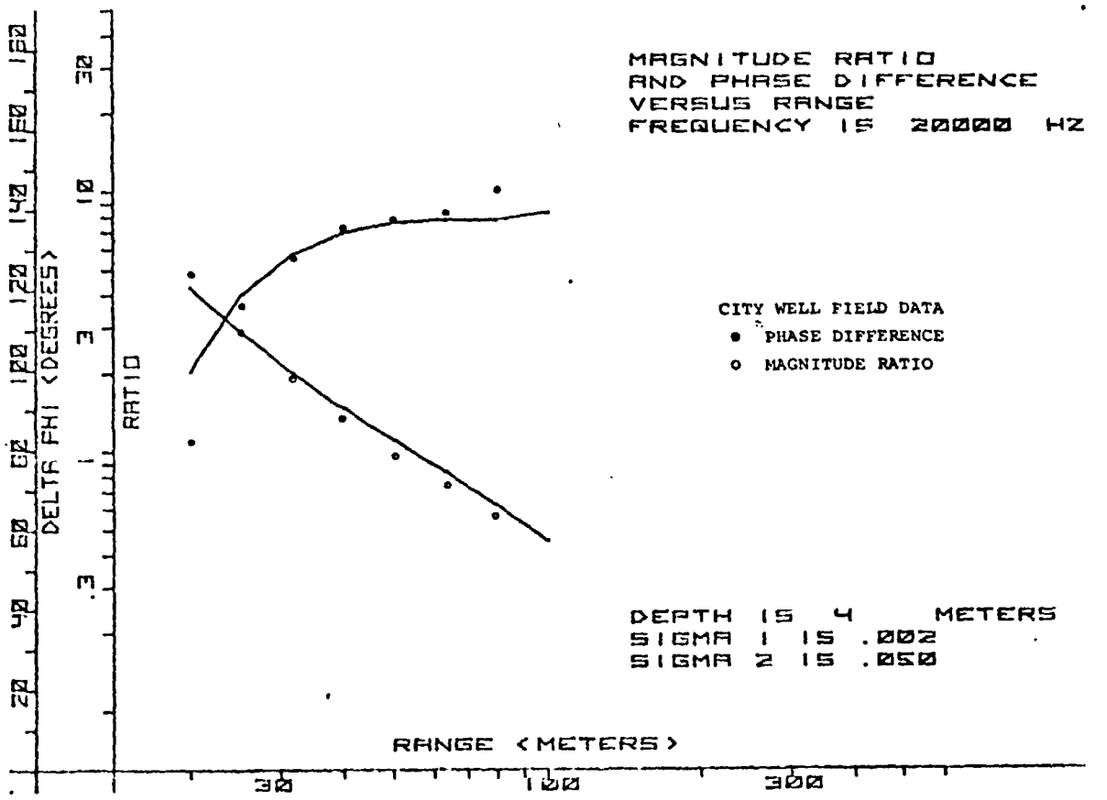

Figure 6-9. Model Curves Compared with City Well Field Data: 20000 Hertz.

6.5 Santa Teresa Mesa Results

Applying the inspection technique outlined in Section 6.2 to the Santa Teresa Mesa data, we can readily infer that the average value of conductivity at the mesa site tends to increase with depth (Figures 6-10 and 6-11). We note in the Mesa data that the ratio curves between the separations of 100 to 200 meters tend to merge on a single curve from which a conductivity of 0.05 can be inferred by matching a half space model to the data curves. Thus, we can assume that a layer of conductivity 0.05 siemens/meter exists at a depth much less than 100 meters. For ranges less than 100 meters, the data curves, though ill defined, seem to approach a conductivity of 0.01 siemens/meter or less and we can deduce that the layer thickness must be less than 25 meters, since the upper layer half space asymptote is not even approached at the separation of 25 meters and the frequencies of 7000 and 16000 hertz. Additionally, we can see that for separations greater than 200 meters, the ratio data curves again tend to translate to the left indicating a third layer of higher conductivity below the 0.05 siemens/meter layer.

Matching half space curves to the data for large separations, we infer a third layer conductivity of 0.1 siemens/meter or larger. We also infer that the third layer is at a depth of the order of 100 meters. We can make this inference because, for a conductivity of 0.05, the skin depth in the second layer is about 70 meters at 400 hertz and about 170 meters at 60 hertz (the two lowest test frequencies) and it would not be possible to sense the third layer at all at depths materially greater than the skin depth in the second layer.

We again plotted our theoretical models in the forms of magnitude ratio and phase difference versus range using the parameter values deduced with our initial inspection technique and compared our model curves with the data.

We found that only 60 hertz was diagnostic of the depth to the third layer whereas the higher frequencies were most diagnostic of the upper layer. After performing several parameter iterations, we deduced the three layer model illustrated in Figure 6-12. The curve matches on which this model is based are presented as Figures 6-13 through 6-18. We interpret the upper thin layer to represent fairly dry soil, the middle layer to represent moist but not saturated soil, and the lower layer to represent saturated soil or the top of the water table. Our interpretation compares favorably with data from nearby wells for which depths of 93 to 102 meters to the water table are reported by Walt Meyer of the U.S.G.S. in El Paso. Additionally, the conductivity values we deduced for this site are consistent with the average conductivity values for the upper 100 meters as reported by Zhody (1969) for test sites in the El Paso area.

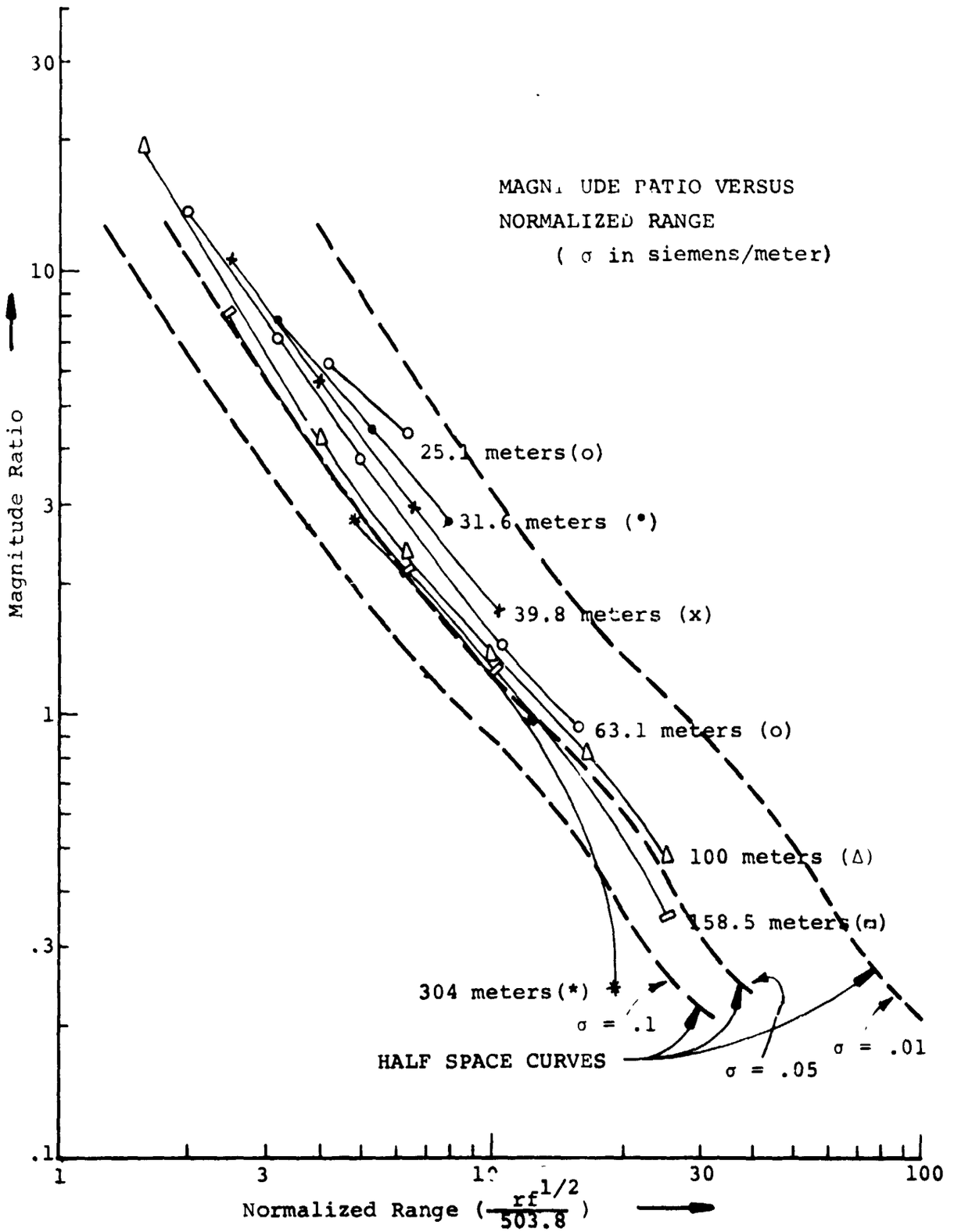

Figure 6-10. Santa Teresa Mesa Data - I

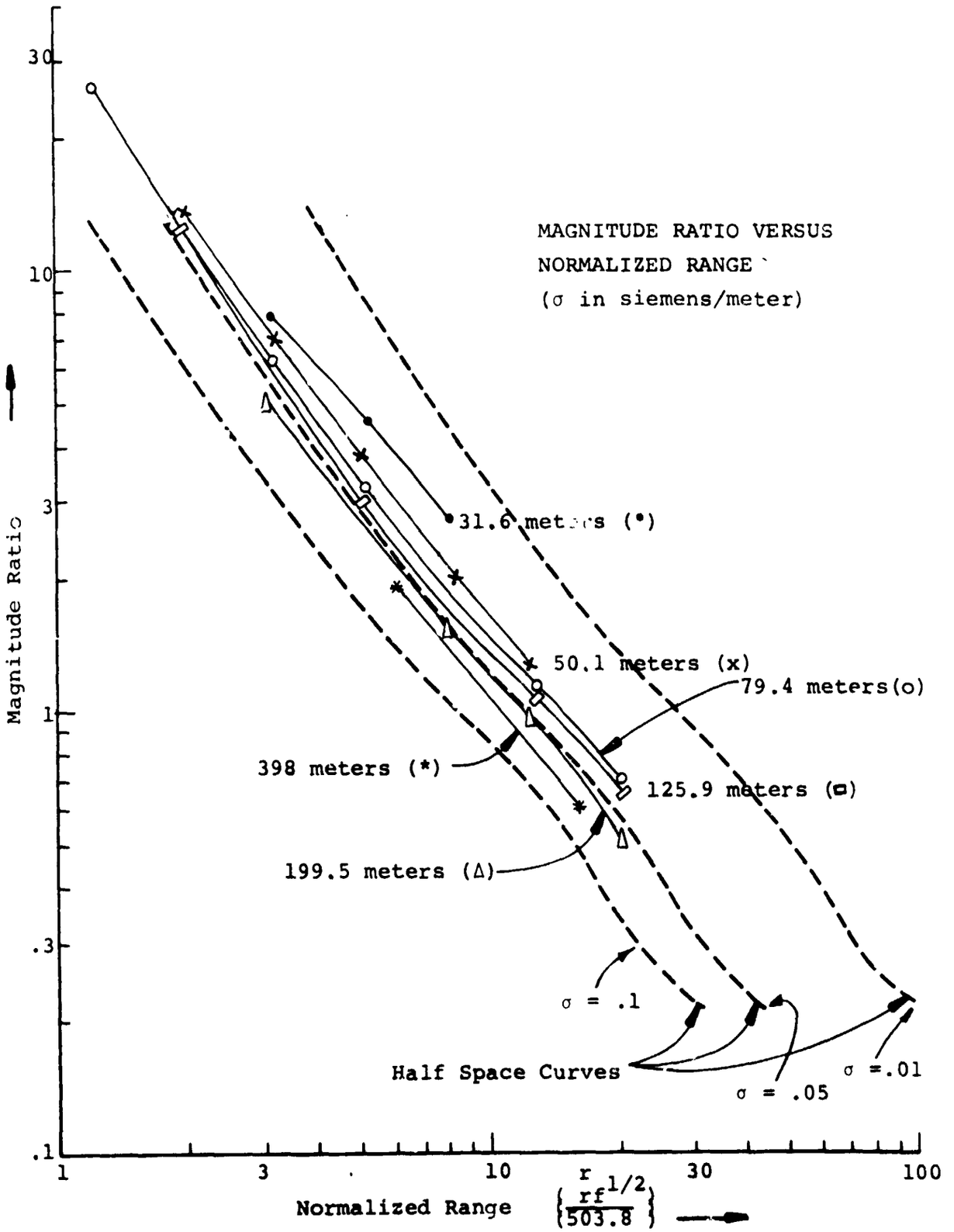

Figure 6-11. Santa Teresa Mesa Data - II

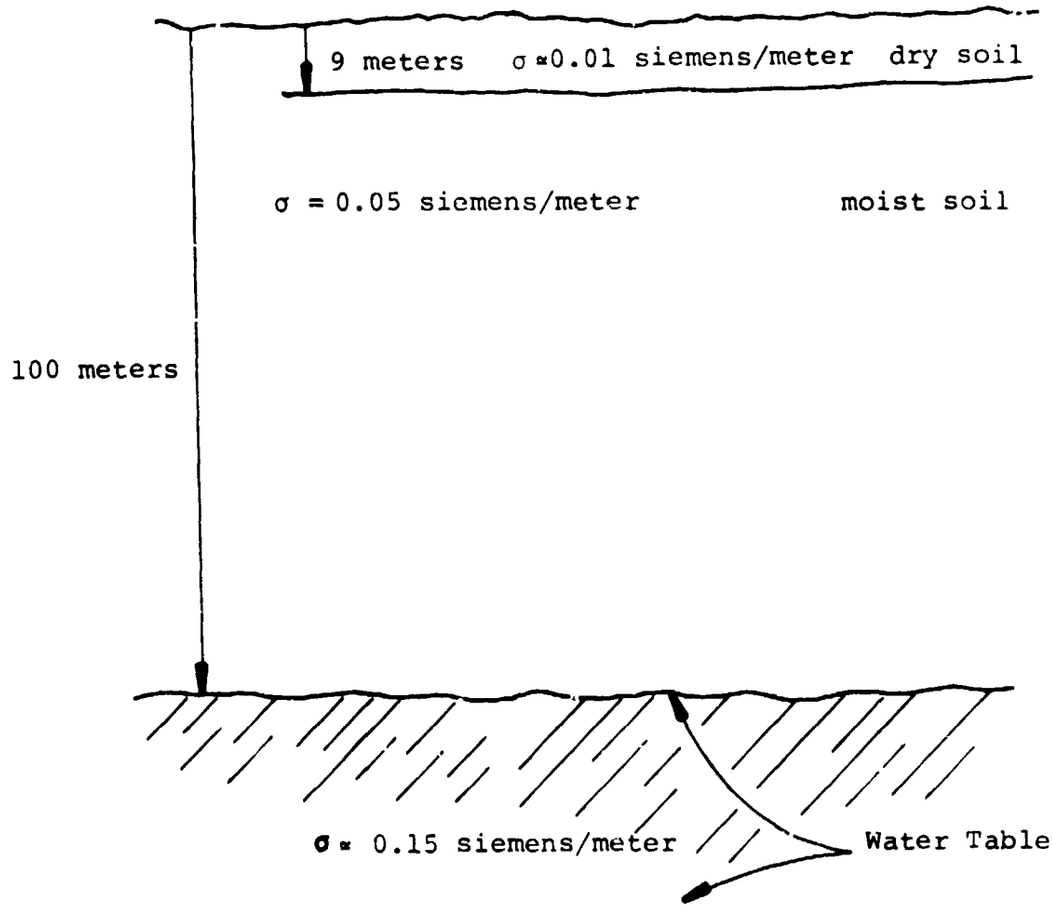

Figure 6-12. Interpreted Conductivity Profile for the Santa Teresa Mesa Test Site

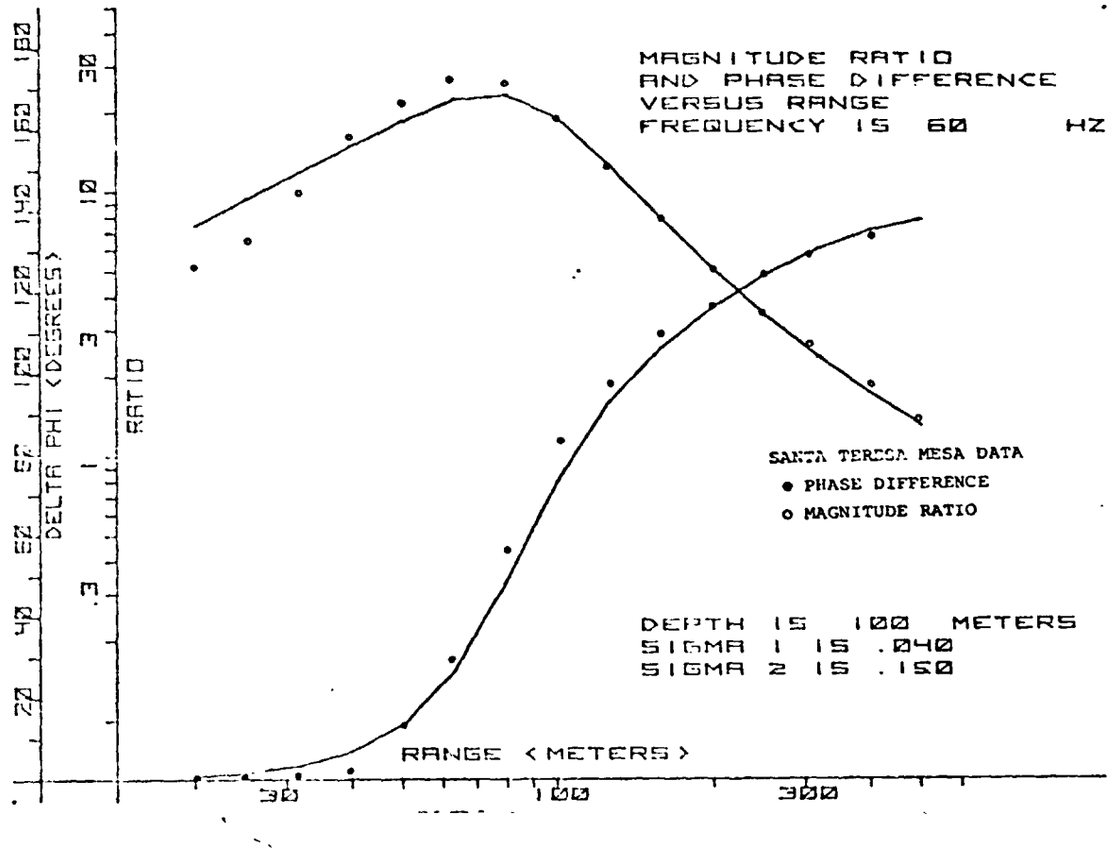

Figure 6-13. Model Curves Compared with Santa Teresa Mesa Data: 60 Hertz.

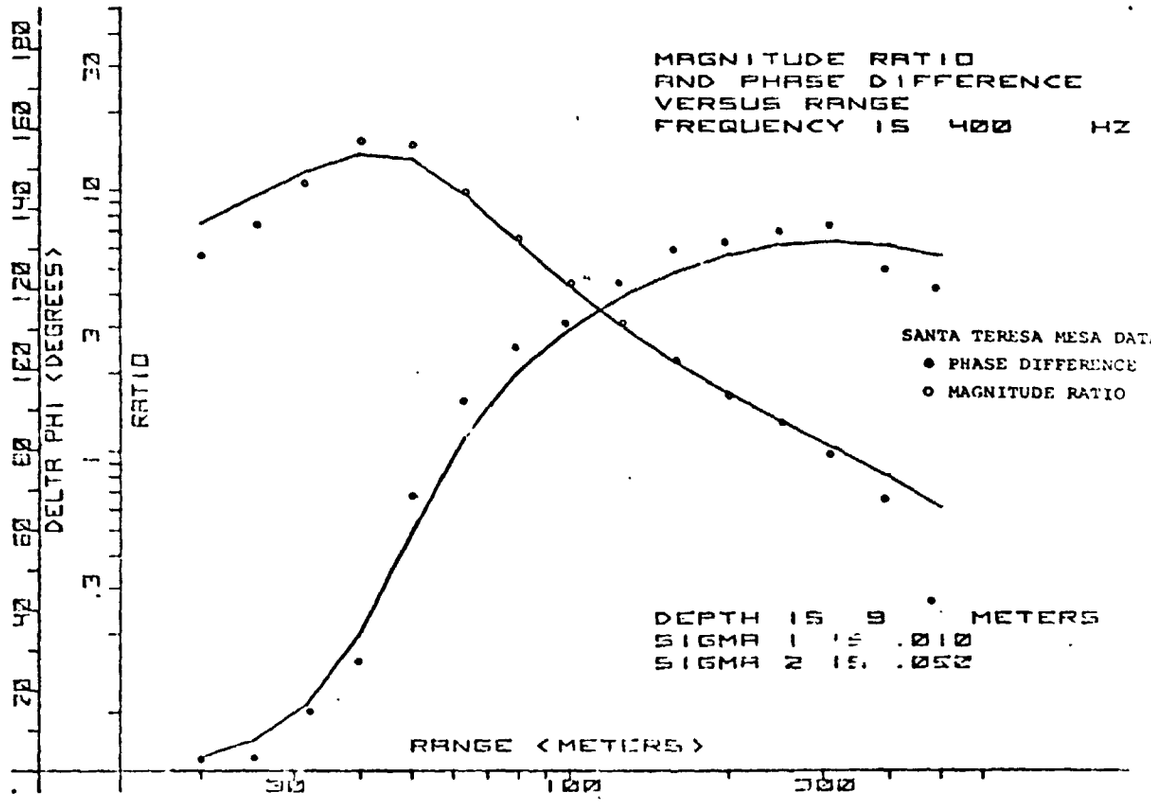

Figure 6-14. Model Curves Compared with Santa Teresa Mesa Data: 400 Hertz.

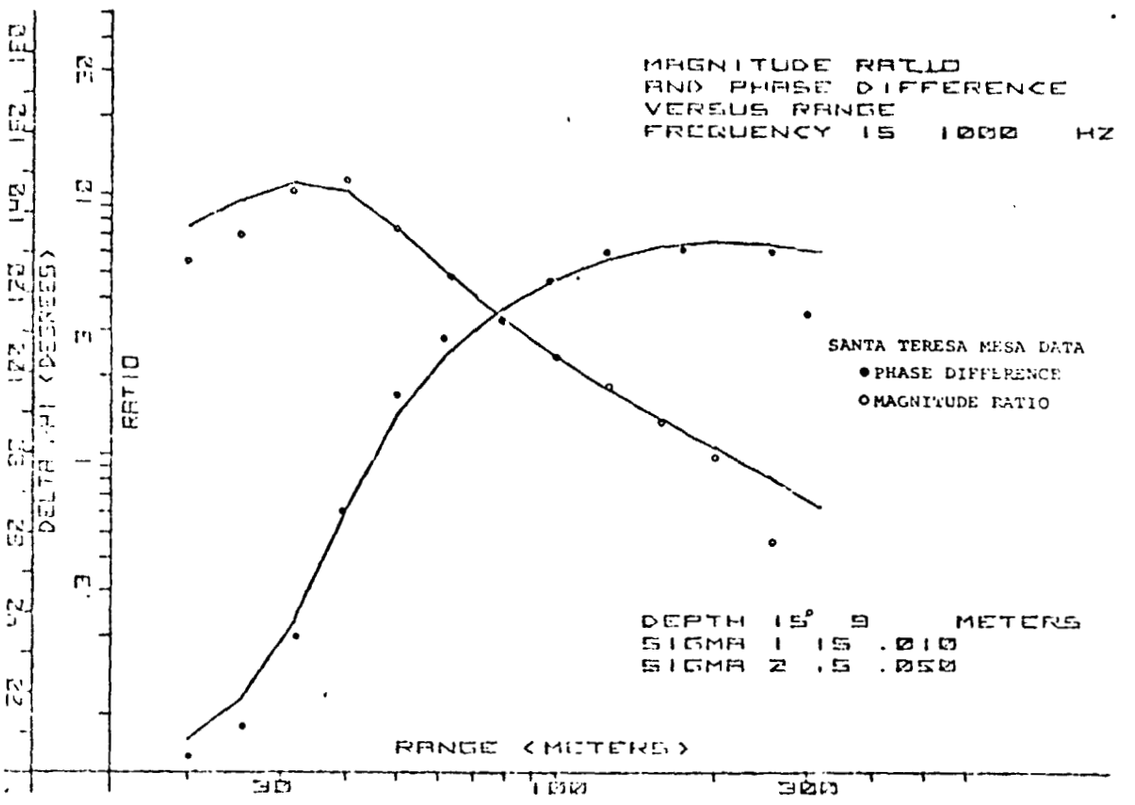

Figure 6-15. Model Curves Compared with Santa Teresa Mesa Data: 1000 Hertz.

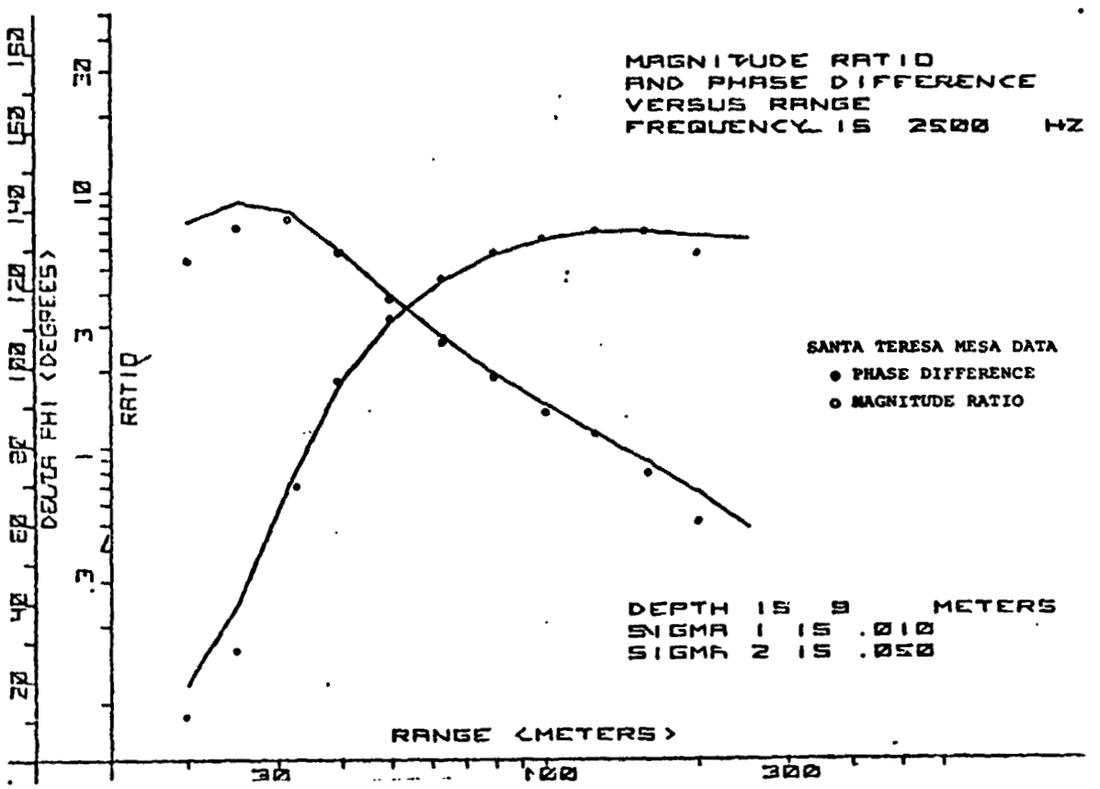

Figure 6-16. Model Curves Compared with Santa Teresa Mesa Data: 2500 Hertz.

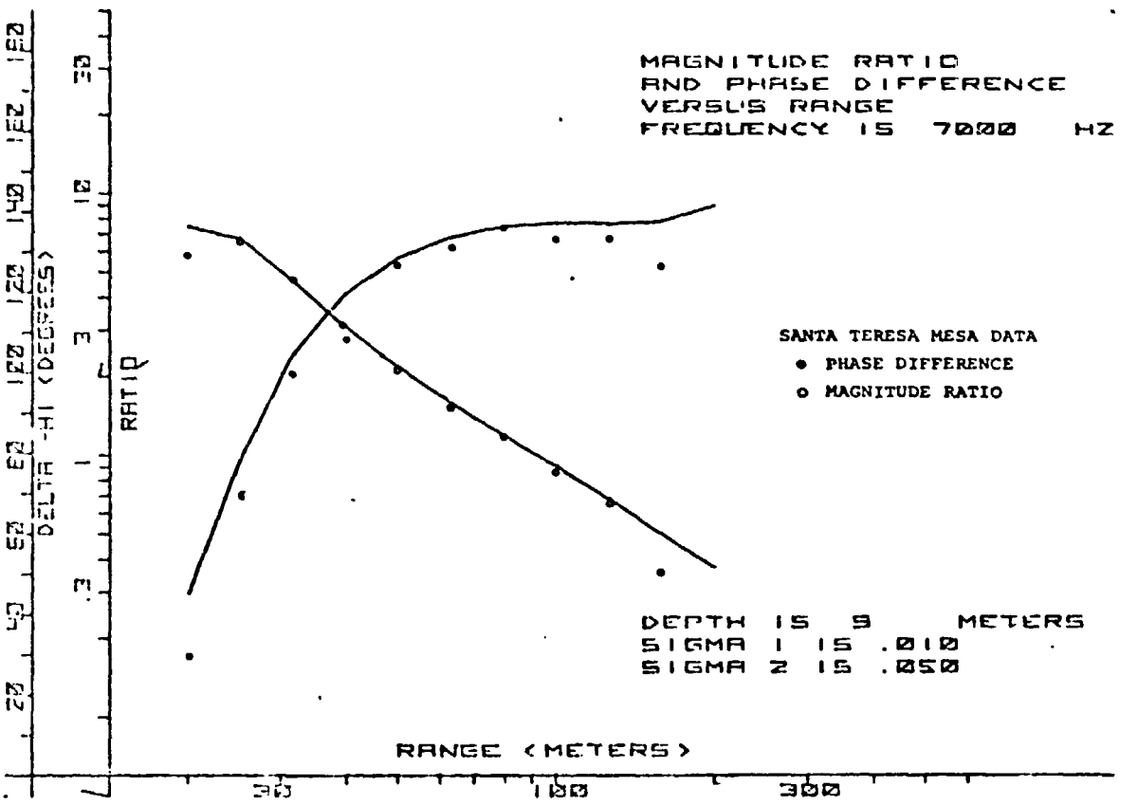

Figure 6-17. Model Curves Compared with Santa Teresa Mesa Data: 7000 Hertz.

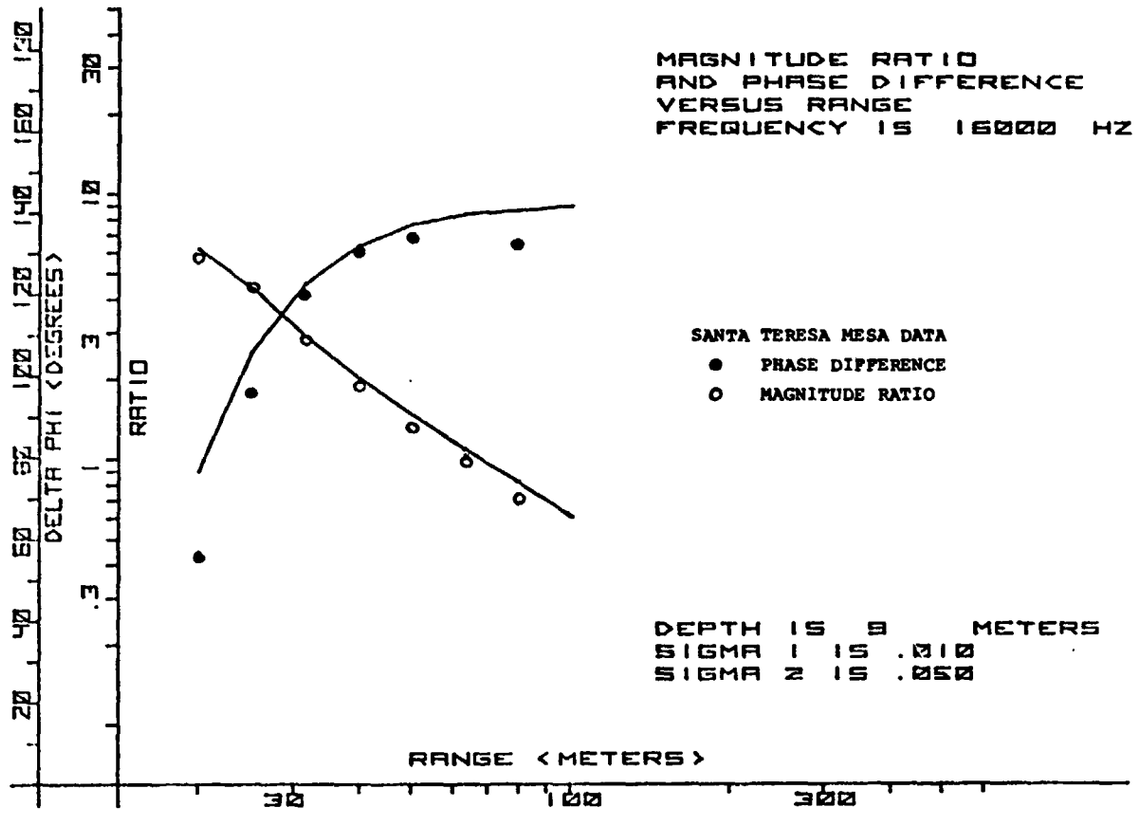

Figure 6-18. Model Curves Compared with Santa Teresa Mesa Data: 16000 Hertz.

6.6 Curve Matching Sensitivity

To clearly illustrate how well our model curves fit the data curves, we now present, as Figure 6-19 through 6-21, overlain model curves representing the effects of perturbing the parameters σ_1, σ_2, and d individually at a source frequency of 1000 Hertz. We should note that we used this iterative process of varying one parameter at a time throughout our study in order to obtain the best possible fit to the data within the limits of our initial assumptions.

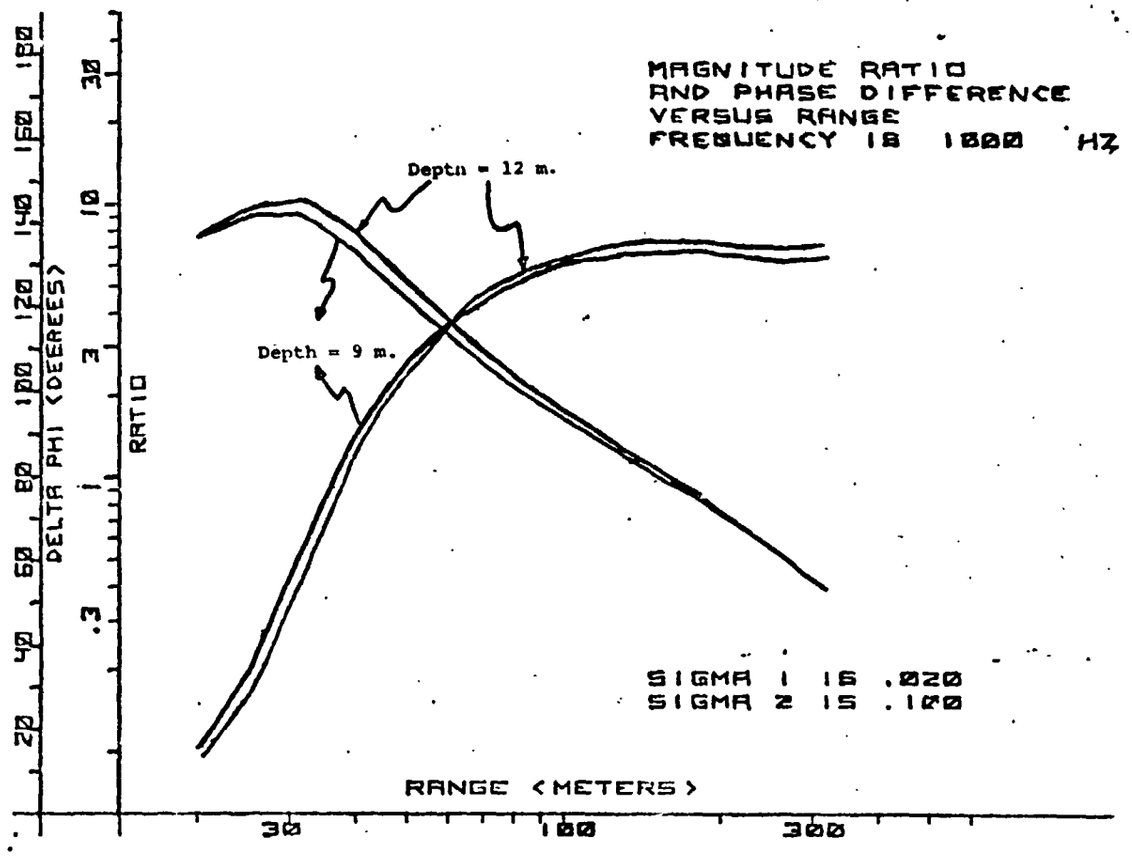

Figure 6-19. Model Magnitude Ratio and Phase Difference versus Range at 1000 Hertz, with Variations in Depth (d).

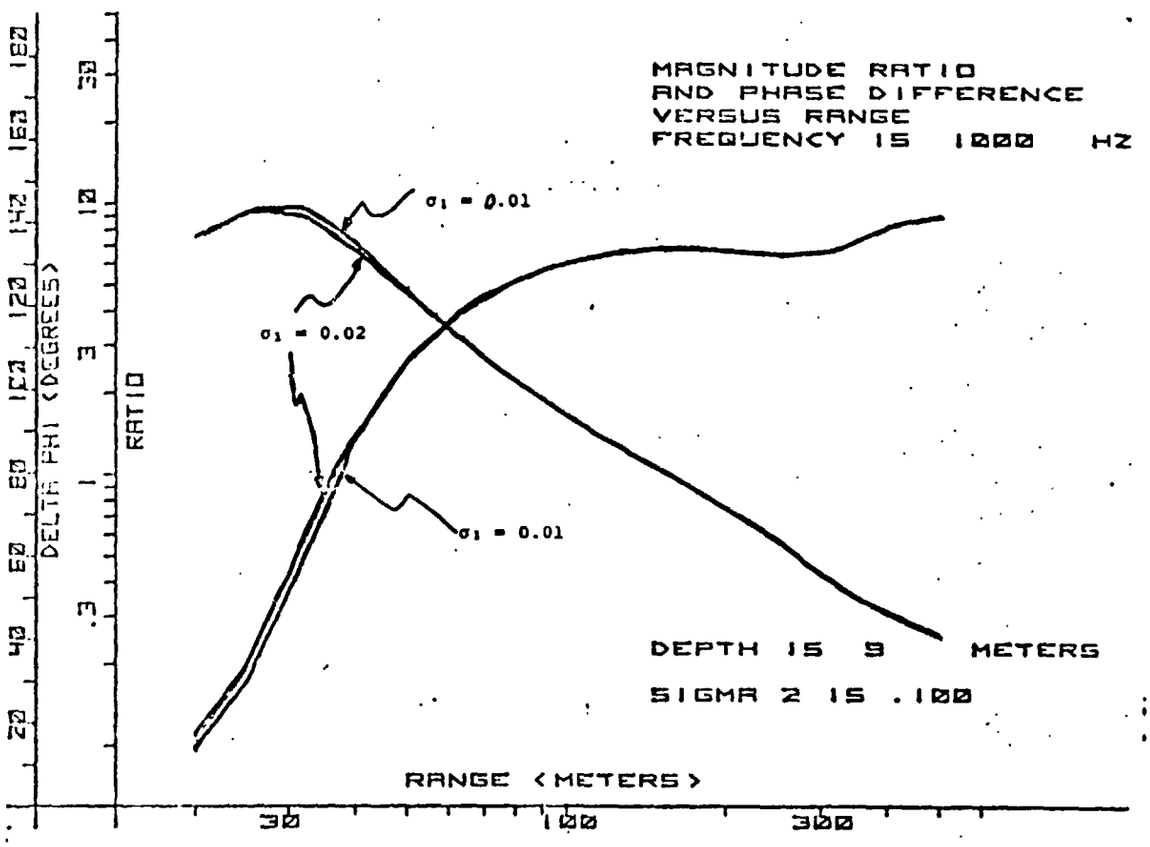

Figure 6-20. Model Magnitude Ratio and Phase Difference versus Range at 1000 Hertz, with Variations in the Conductivity of the Upper Layer (σ_1).

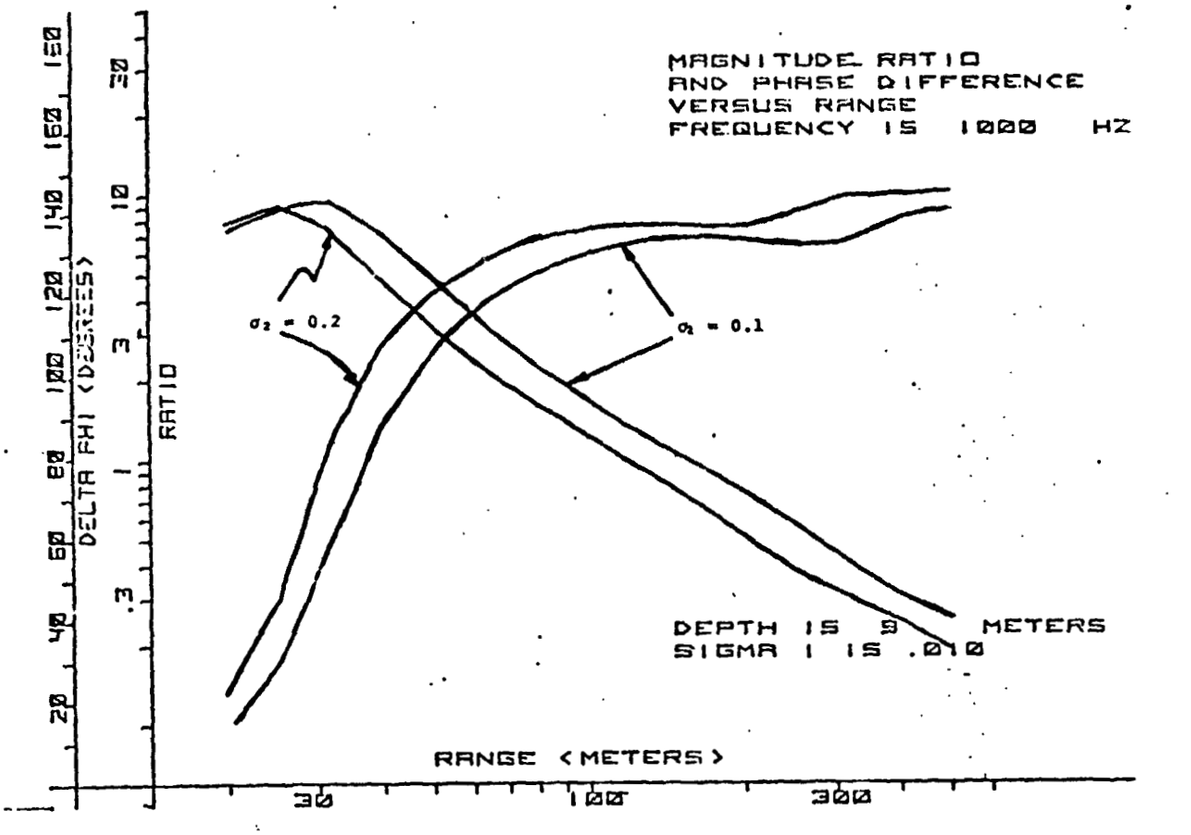

Figure 6-21. Model Magnitude Ratio and Phase Difference versus Range at 1000 Hertz, with Variations in the Conductivity of the Lower Layer (σ_2).

7.0 Recommendations

There seems now to be little doubt that the inductive coupling technique can be developed into a practical system for the quick and definitive determination of subsurface conductivities at depths extending to a few hundred meters. And, because subsurface water in arid regions usually results in sharp conductivity contrasts that are particularly easy to detect, this technique shows promise as a useful tool for mapping large regions in order to identify specific places from which subsurface water might be recovered economically.

Work which needs to be done to bring this system to fruition includes extension of the theory to nonhomogeneous situations, the development of rapid interpretation procedures suitable for real time use in the field, the fabrication of automated operational hardware, and field tests designed to test the system thoroughly in a realistic environment. These various items are discussed below.

7.1 Theoretical Analysis

We chose to conduct the initial feasibility test in a geologically simple area where the subsurface structure was known to be homogeneous and isotropic, and to have only two or three layers. This made possible several simplifying assumptions in the theoretical work which, consequently, may not be applicable to all areas of potential interest.

The theoretical work should be continued, therefore, in order to generalize the theory to more complicated geological structures having many layers that are not uniform, and to structures better characterized by

continuous gradations of conductivity rather than discrete layers.

Additionally, in our data interpretation and analysis we used a large computer facility to make lengthy (and expensive) numerical integrations in order to generate specific model curves which we then compared with plots of the experimental data. This forward, curve matching, procedure initially had great advantage because it illuminated some discrepancies and biasses in the data, it directed our efforts toward the selection of reasonable models, and it enabled us to make judgements about the validity of some approximations and about the rigor with which numerical computations had to be performed.

However, using a large computer to generate specific model curves which are later compared with the experimental data obviously is not a long term solution to the problem. The procedure is cumbersome and does not make efficient use of the computer capabilities; it requires a great deal of intuitive, and subjective, manual intervention; and it is clearly not suitable for real time data interpretation in the field.

Work needs to be done in this area, therefore, to develop direct data inversion techniques (as outlined in Appendix C), to simplify the numerical calculations (as outlined in Appendix B), to generate catalogs of curves and to identify specific features of the data yielding rapid approximations to the subsurface conditions. And, importantly, this additional theoretical work is needed to help define system operating procedures that maximize the amount of interpretable data collected with a given expenditure of time and effort in the field.

7.2 Operational Procedure

The ultimate SWEEP system will employ two self-propelled vehicles, one carrying the source and one carrying the detector, which can move independently through a region that is to be mapped.

With both vehicles stopped, data can be collected in a form convenient for immediate interpretation by sweeping the signal frequency or by varying the frequency in discrete steps. Additionally, data can be collected as the separation between the vehicles is changed or as both vehicles move simultaneously along, or parallel to, a traverse line.

With this many degrees of freedom, there obviously is opportunity for considerable ingenuity in devising an optimum operational routine that permits the rapid identification of areas of likely interest and the subsequent checking of postulated models.

7.3 Equipment

In previous attempts to exploit the inductive coupling prospecting technique, one of the most difficult hardware problems, and, indeed, the one which usually has been an intolerable handicap, has been the implementation of a high power, variable frequency, source power supply. To provide a large enough system signal-to-noise ratio to permit measurements to depths of the order of a few hundred meters it is necessary to drive the source coil with currents in the order of 50 amperes at power levels in the order of 15 kilowatts at frequencies ranging down to about 10 hertz.

In Appendix E, we describe a technique for solving this problem. A switched source synthesizer, developed

for another purpose, makes possible a very efficient DC-to-AC inverter that creates a quasisinusoid by connecting storage batteries in series-parallel combinations. Since the full system power for SWEEP is required only in short spurts, just long enough to obtain a datum point, the storage batteries can be recharged with no difficulty from a modest sized, continuously running, prime power source such as a gasoline driven alternator. The switched source synthesizer technique described in Appendix E, therefore, makes the small, high power, low frequency, portable power source a practical reality.

As part of an operational system, we shall need a coherent detector of a form similar to that used in the initial feasibility trials, and a telemetry link to ensure that the source and detecting vehicles operate in unison. These items, however, require no technological advances but can be implemented readily with existing hardware techniques.

7.4 Field Trials

To date, we have obtained field data only from two sites near El Paso, Texas. This experience should be extended as soon as possible, preferably by progressing from areas with well known geology to surveys of the unknown.

Experience during the initial feasibility test showed (once again) that a great deal of time can be wasted fixing engineering problems in the field. For this reason the field trials should be conducted with a well engineered, reliable, system that has been thoroughly tested prior to the actual field trials. Presently we think that we should instrument a pair of vehicles, one for the source and one for the receiver, and perform three local

shakedown engineering tests before embarking on full scale field trials elsewhere.

8.0 Acknowledgments

The authors wish to acknowledge with appreciation the contributions made by Professor John V. Harrington, who first suggested the adaptation of the Surface Electrical Properties sounding technique to terrestrial applications and formulated the theoretical approach; by Professor Jack Ruina for his suggestions about possible applications in African drought areas and his authorization for partial funding support; by Professor Gene Simmons for his guidance in site selection and assistance with field trials; by Richard H. Baker for his assistance with equipment design; by Dr. James W. Meyer for his review of the manuscript; by Frank Miller who contributed his engineering expertise and good humor to the preparation and execution of the El Paso field trial; and by Walter Meyer at the El Paso, Texas, office of the United States Geological Survey for his advice on local sites and data on water depths and quality.

We also wish to thank Larry Beckley, Dr. Joe DeBettencourt, Dr. Paul Kasameyer, Professor Jin Au Kong, and Professor Ted Madden, who were kind enough to read the final draft and offer constructive criticism. Their comments enabled us to improve the report and we regret that budget considerations prevented us from incorporating all of their suggestions.

Calculations were performed on the IBM S/370 computer facility of the MIT Information Processing Center.

Financial support for the project was provided jointly under NASA Headquarters Grant NGL 22-001-019 and by the U.S. Department of State, Agency for International Development, Grant AID/csd-3360.

9.0 References

F.C. Frischknecht, "Fields about an oscillating magnetic dipole over a two layer earth and application to ground and airborne electromagnetic surveyw," Quarterly of Colorado School of Mines, 62(1), pp. 370, 1967.

W.E. Glenn, et al, "The inversion of vertical magnetic dipole sounding data," Geophysics, 38(6), pp. 1109-1129, 1973.

J.V. Harrington, Personal communication, 1973.

R.W.P. King and C.W. Harrison, Jr., "Antennas and Waves," MIT Press, 1969.

J.A. Kong, "Electromagnetic Fields due to Dipole Antennas over Stratified Anisotropic Media," Geophysics, Vol. 37, No. 6, pp. 985-996, Dec. 1972.

E.R. Leggat, M.E. Lowry, and J.W. Hood, "Ground-water resources of the Lower Mesilla Valley Texas and New Mexico," Geol. Survey Water-Supply Paper, 1969-AA, 1963.

I.M. Longman, "Tables for the rapid and accurate numerical evaluation of certain infinite integrals involving Bessel functions," Mathematical Tables and Other Aids to Computation, 11(59), pp. 166-180, 1957.

T.R. Madden, "Transmission systems and network analogies to geophysical forward and inverse problems," ONR Technical Report, MIT Report No. 72-3, 1972.

W. Meyer, Personal communication, 1973.

S. Ryu et al, "Electromagnetic fields about a loop source of current," Geophysics, 35(5), pp.862-896, 1970.

G. Simmons, D.W. Strangway, L. Bannister, D. Cubley, and G. LaTorraca, "The Surface Electric Properties Experiment," The Moon, 6, 258, 1973.

L.B. Slichter and L. Knopoff. "Field of an alternating magnetic dipole on the surface of a layered earth," Geophysics, 24(1), pp.77-88, 1959.

D.W. Strangway, G. Simmons, R. Watts, G. LaTorraca, L. Bannister, R. Baker, J.E. Redman, and J.R. Rossiter, "Radio Frequency Interferometry--A New Technique for Study of Glaciers," J. Glaciology, 1972.

L. Tsang, J.A. Kong, and Gene Simmons, "Interference Patterns of a Horizontal Electric Dipole over Layered Dielectric Media," J. Geophysical Research, June 1973.

J.R. Wait, "The magnetic dipole over the horizontally stratified earth," Canadian Journal of Physics, Vol 29, pp. 577-592, 1951.

J.R. Wait, "Mutual coupling of loops lying on the ground," Geophysics, Vol. 19, pp. 290-296, 1954.

J.R. Wait, "Induction by an oscillating magnetic dipole over a two layer earth," Applied Science Research, Section B, 7:73-80, 1958.

J.R. Wait and J.A. Fuller, "Argand representations of the mutual electromagnetic coupling of loops on a two layer earth," Geoexploration, 10:221-227, 1972.

J.R. Wait, "Image theory of a quasi-static magnetic dipole over a dissipative half space," Elect. Lett., 5(13), pp. 281-282, 1969.

J.R. Wait, "Electromagnetic waves in stratified media," Pergamon Press, 8-20, 1962 and 1970.

S.H. Ward, "Electromagnetic theory for geophysical application," Mining Geophysics, Vol. 2:Tulsa SEG, 1967.

J.T. Weaver, "Image theory for an arbitrary quasi-static field in the presence of a conducting half space," Radio Science, Vol. 6, pp. 647-643, 1971.

J.T. Weaver, "The general theory of electromagnetic induction in a conducting half space," Geophysics, Vol. 22, 1970.

A.R. Zhody, "The Use of Schlumberger and equatorial soundings in ground water investigations near El Paso, Texas," Geophysics, Vol. 34, pp. 713-728, 1969.

"Surface Electrical Properties Experiment" Final report, NASA contract NAS 9-11540, MIT Reports Nos. CSR-TR-73-4, CSR-TR-74-2, CSR-TR-74-1.

Appendix A: Multilayer Analysis

In chapter 4 we described the analysis and calculation of the magnetic field induced by a magnetic dipole over a two layer earth. The mathematical procedures of Chapter 4 of matching boundary conditions for the Hertz vector and solving simultaneous equations for the reflection and transmission coefficients could be extended to three or more layers. However, a simpler approach is to put the wave equations into the form of transmission line equations, considering each layer as a cascaded segment of a transmission line.

Ward (1967) applied the transmission line analogy to a loop over a multilayer medium and his results are listed below.

As in equations (4.19) and (4.20) we can write expressions for H_z and H_r for a current loop on a multilayered conducting earth, as shown in Figure 4-1, in the forms:

$$H_z = \frac{m}{4\pi}\int_0^\infty R(\lambda)\ \lambda^2\ J_0(\lambda r)\ e^{-\lambda z}\ d\lambda \qquad \text{(A.1)}$$

and:

$$H_r = \frac{m}{4\pi}\int_0^\infty R(\lambda)\ \lambda^2\ J_1(\lambda r)\ e^{-\lambda z}\ d\lambda \quad (e^{+i\omega t}\ \text{implied}) \qquad \text{(A.2)}$$

where:

$$R(\lambda) + 1 = \frac{K_0}{K_0 + Z_0} \qquad \text{(A.3)}$$

$$Z_0 = K_1\ \frac{Z_1 + K_1 \tanh \alpha_1 d_1}{K_1 + Z_1 \tanh \alpha_1 d_1} \qquad \text{(A.4a)}$$

- -

$$Z_{n-1} = K_n\ \frac{Z_n + K_n \tanh \alpha_n d_n}{K_n + Z_n \tanh \alpha_n d_n} \qquad \text{(A.4b)}$$

- -

$$Z_{i-1} = K_i \qquad \text{(A.5)}$$

where K_i is the characteristic impedance of each layer and is represented by the equation;

$$K_i = -\frac{i\omega\mu_0}{\alpha_i} \qquad \text{(A.6)}$$

where:

$$\alpha_i = (\lambda^2 + i\sigma_i\mu_0\omega)^{\frac{1}{2}}$$

Thus we have presented expressions for the magnetic field components induced by a magnetic dipole (current loop) over a multilayered earth. These expressions can be solved numerically using the techniques of section 4.3. However, for future work we propose the use of the simpler, less costly, numerical technique described in Appendix B.

Appendix B: Integral Approximation

We recall from Appendix A that the multilayer integral forms for the magnetic field H_z and H_r can be written as:

$$H_z = \frac{m}{4\pi} \int_0^\infty \lambda^2 J_0(\lambda r)\ e^{-\lambda z}\ R(\lambda)\ d\lambda \qquad (B.1)$$

and:

$$H_r = \frac{m}{4\pi} \int_0^\infty \lambda^2 J_1(\lambda r)\ e^{-\lambda z}\ R(\lambda)\ d\lambda \qquad (B.2)$$

Madden (1974) has simplified the numerical integration of equations of these forms by defining the kernel $R(\lambda)$ in the series form:

$$R(\lambda) \equiv \sum_i e^{-b_i \lambda}\ a_i \qquad (B.3)$$

where b_i are a preselected set of coefficients the specification of which is based on the expected range of values of λ for a given source receiver separation and conductivity-layering model.

Now, we can write H_z (or similarly H_r) in the form:

$$H_z = \frac{\partial^2}{\partial z^2} \int_0^\infty \sum_i e^{-b_i \lambda}\ a_i\ J_0(\lambda r)\ e^{-\lambda z}\ d\lambda \qquad (B.4)$$

Reversing the order of integration and summation we have:

$$H_z = \sum_i a_i \frac{\partial^2}{\partial z^2} \int_0^\infty e^{-(b_i+z)\lambda} J_0(\lambda r)\, d\lambda$$

$$= \sum_i a_i \left\{ \frac{3b_i^2}{(r^2+b_i^2)^{\frac{5}{2}}} - \frac{1}{(r^2+b_i^2)^{\frac{3}{2}}} \right\} \qquad (B.5)$$

and if we define the elements of the vector a as a_i and the vector c as c_i where:

$$c_i = \left\{ \frac{3b_i^2}{(r^2+b_i^2)^{\frac{5}{2}}} - \frac{1}{(r^2+b_i^2)^{\frac{3}{2}}} \right\} \qquad (B.6)$$

we can write:

$$H_z = a^T c \qquad (B.7)$$

The next step, then, is to determine the vector a.

Recalling, from B.3, that:

$$R(\lambda) \equiv \sum_i e^{-b_i\lambda} a_i$$

and making the approximation that the continuous function $R(\lambda)$ can be represented by a discrete set of $R(\lambda_j)$ which span the necessary range of values of λ for an accurate approximation to the integral, we can write:

$$R(\lambda) \simeq R(\lambda_j) = \sum_i e^{-b_i \lambda_j} a_i \qquad (B.8)$$

and in matrix notation:

$$R_j = B_{ij} a_i \qquad (B.9)$$

or

$$R = Ba$$

To find the vector a we premultiply both sides of equation (B.9) by $B=(B^*)^T$ such that:

$$\hat{B}R = \hat{B}B\alpha \qquad (B.10)$$

and:

$$a = (\hat{B}B)^{-1} \hat{B}R \qquad (B.11)$$

where:

B^* is the conjugate of B

$B = (B^*)^T$ is the transpose of B^*

and the use of $\hat{B}$ insures a unique matrix inversion to find a.

Accordingly we can write:

$$H_z \cong \left[(\hat{B}B)^{-1} \hat{B}R\right]^T c \qquad (B.12)$$

Thus, we have a least squares approximation to the solution of the forward problem which can be used to reduce computation time drastically. An additional attraction to this shortcut integration approach is that much of the computation can be reused for the calculations of the data derivatives necessary for the implementation of the inversion scheme described in Appendix C.

Appendix C: Data Inversion

Data inversion is an iterative process in which perturbations in the parameters of a theoretical model are used to minimize, in the least squares sense, differences between the calculated model values and the actual data.

If the theoretical model closely approximates the physical situation, we can write:

$$H_z(\text{measured}) = H_z(\text{model})) + \frac{\partial H_z}{\partial p_i} (p_i - p(\text{model})) \qquad (C.1)$$

where $(p_i - p(\text{model}))$ are the variations from the original model necessary to fulfill the equality of (C.1), or in matrix form:

$$\Delta H = H_z(\text{measured}) - H_z(\text{model}) = \frac{\partial H_z}{\partial p_i} \Delta p \qquad (C.2)$$

and in the equal parameter weighting form:

$$\ell n \left\{ \frac{H_z(\text{measured})}{H_z(\text{model})} \right\} = \frac{\partial (\ell n\, H_z(\text{model}))}{\partial (\ell n\, p_i)} \Delta \ell n\, p_i \qquad (C.3)$$

where p_i represents the i unknown parameter values of the model. Consequently, we have a set of equations in the matrix form

$$Ay = d$$

where y represents the variations in the parameters

d the difference between observed and calculated H_z

and A the general m by n sensitivity matrix of the partial derivatives of the model equations with respect to the unknown parameters.

We wish to find y for which d goes to zero or a minimum. Thus, we need to find the generalized inverse of A in terms of a set of non-zero eigenvalues.

Following Professor Madden's course notes (1974), we find the generalized inverse to be of the form:

$$y = (\tilde{A}A + \varepsilon^2 E)^{-1} \tilde{A}\, d \qquad (C.4)$$

where E is the unit matrix and ε is an arbitrary bias term necessary to prevent overemphasis of near zero eigenvalues of $\tilde{A}A$.

Briefly, the above inverse formulation circumvents inversion difficulties due to small or zero eigenvalues and squelches non-unique and incompatible solutions. The determination and iteration of the eigenvalues of the matrix A is the key factor in the realization of data inversion, since as we change y to minimize d, the matrix A also changes. We shall show now that much of the calculation of the sensitivity matrix has already been accomplished in the solution to the forward problem as calculated in Appendix B.

C.1 Sensitivity Matrix Calculations

Recalling from Appendix A that the vertical magnetic field H_z can be represented as:

$$H_z = \int_0^\infty R(\lambda)\, J_0(\lambda r)\, \lambda^2\, e^{-\lambda z}\, d\lambda \qquad (C.5)$$

and noting that all the information for the partials of H_z with respect to the unknown parameters σ_i and d_i is in the kernel $R(\lambda)$, we can write:

$$\frac{\partial H_z}{\partial p_i} = \int_0^\infty \frac{\partial R(\lambda)}{\partial p_i} J_0(\lambda r)\ \lambda^2\ e^{-\lambda z}\ d\lambda \qquad (C.6)$$

where p_i represents the unknown parameters σ_i and d_i. Recalling from Appendix B that:

$$H_z = a^T c \qquad (C.7)$$

we can write the approximate sensitivity matrix as:

$$\frac{\partial H_z}{\partial p_i} = \frac{\partial}{\partial p_i}\ (a^T c) = \left\{ (\tilde{B}B)^{-1}\ \tilde{B}\ \frac{\partial R}{\partial p_i} \right\}^T\ c \qquad (C.8)$$

Thus, for each forward problem solution we can readily determine the corresponding sensitivity matrix, if we can analytically determine the partials of $R(\lambda)$ with respect to the parameters d_i and σ_i.

Instead of finding the partials of $R(\lambda)$ directly, we shall find the partials of $1+R(\lambda)$ which is a simpler form to differentiate. We shall show that the partial differentials can be put in a simple recursive form so that the partial derivative with respect to any layer thickness or conductivity may be found easily.

C.2 Recursive Differentials

Recalling from Appendix A that:

$$R(\lambda) + 1 = \frac{K_0}{K_0 + Z_0} \tag{C.9}$$

and differentiating with respect to the layer thickness d_1, we find

$$\frac{\partial R(\lambda)}{\partial d_1} = -K_0 \, (K_0 + Z_0)^{-2} \, \frac{\partial Z_0}{\partial d_1}$$

$$= \frac{-\alpha_1 K_0 K_1}{(K_0+Z_0)^2} \left\{ \frac{(K_1^2 - Z_1^2)(\text{sech}^2 \, \alpha_1 d_1)}{(K_1 + Z_1 \, \tanh \, \alpha_1 d_1)^2} \right\} \tag{C.10}$$

We can deduce immediately from equations (C.10) and (A.4) that the general expression for $\partial Z_i / \partial d_{i+1}$ is of the form:

$$\frac{\partial Z_i}{\partial d_{i+1}} = \alpha_{i+1} \, K_{i+1} \left\{ \frac{(K_{i+1}^2 - Z_{i+1}^2)(\text{sech}^2 \, \alpha_{i+1} d_{i+1})}{(K_{i+1} + Z_{i+1} \, \tanh \, \alpha_{i+1} \, d_{i+1})^2} \right\} \tag{C.11}$$

Noting that we can put the partial derivative of $R(\lambda)$ with respect to any layer (i+1) in the form:

$$\frac{\partial R(\lambda)}{\partial d_{i+1}} = \left[\frac{-K_0}{(K_0+Z_0)^2} \right] \left[\frac{\partial Z_0}{\partial d_{i+1}} \right] = \left[\frac{-K_0}{(K_0+Z_0)^2} \right] \frac{\partial Z_0}{\partial Z_1} \frac{\partial Z_1}{\partial Z_2} \cdots \frac{\partial Z_i}{\partial d_{i+1}} \tag{C.12}$$

we see that a general form of the partials $\partial Z_i / \partial Z_{i+1}$ is necessary to allow a general expression for the partials of $R(\lambda)$ with respect to layer thicknesses.

Noting that we can write the partial of Z_0 with respect to Z_1 in the form:

$$\frac{\partial Z_0}{\partial Z_1} = \frac{K_1^2(1 - \tanh^2 \alpha_1 d_1)}{(K_1 + Z_1 \tanh \alpha_1 d_1)^2} \tag{C.13}$$

and again inspecting equation (A.4), we can easily deduce the generalization of (C.13) as:

$$\frac{\partial Z_i}{\partial Z_{i+1}} = \frac{K_{i+1}^2 (1 - \tanh^2 \alpha_{i+1} d_{i+1})}{(K_{i+1} + Z_{i+1} \tanh \alpha_{i+1} d_{i+1})^2} \tag{C.14}$$

Accordingly, we can write equation (C.12) in the general form:

$$\frac{\partial R(\lambda)}{\partial d_{i+1}} = \frac{-K_0}{(K_0+Z_0)^2} \left\{ \prod_{i=0}^{i-1} \frac{\partial Z_i}{\partial Z_{i+1}} \right\} \frac{\partial Z_i}{\partial d_{i+1}}$$

$$= \frac{-K_0}{(K_0+Z_0)^2} \left\{ \prod_{i=1}^{i} \frac{K_i^2(1 - \tanh^2 \alpha_i d_i)}{(K_i + Z_i \tanh \alpha_i d_i)^2} \right\}$$

$$\left\{ \frac{\alpha_{i+1} K_{i+1} (K_{i+1}^2 - Z_{i+1}^2) \operatorname{sech}^2 \alpha_{i+1} d_{i+1}}{(K_{i+1} + Z_{i+1} \tanh \alpha_{i+1} d_{i+1})} \right\}$$

(C.15)

Thus, using the above recurrence relationships for the partials of $R(\lambda)$ with respect to d_i, we can readily determine all the derivatives of d_i.

Recurrence relationships for the partial derivatives of $R(\lambda)$ with respect to the conductivities σ_i can be similarly obtained with the realization that σ_i is implicit in the characteristic impedances K_i as well as the port impedances Z_i.

The solution posed herein should reduce the amount of computer time necessary for the inversion of data for the simple geologic case of one dimensional layering. However, more work must be done to determine the interdependence of σ_i and d_i and the optimum iterative scheme for achieving data inversion.

Appendix D: The Image Approximation for a Multilayered Earth

Wait (1969) and Weaver (1971) developed approximate solutions for the electromagnetic fields of a magnetic dipole over a conducting half-space. Earlier, Wait (1962 and 1970) had developed expressions for a line source over a conducting layered medium. Additionally, Harrington (1973) suggested that the image approximation could be extended to the determination of the magnetic field of a magnetic dipole over a multilayered, conducting earth with the introduction of a "stratified image depth", alpha α. In this appendix, we shall outline the mathematical basis for Harrington's extension following the analyses of Wait (1962, 1969). We shall change our notation in this appendix to distinguish the α_i of Chapter 4 from the image depth α.

Consider a magnetic dipole of moment m at a height h above a multi-layered conducting earth spanned by the coordinate system (r,z) as illustrated in Figure D-1.

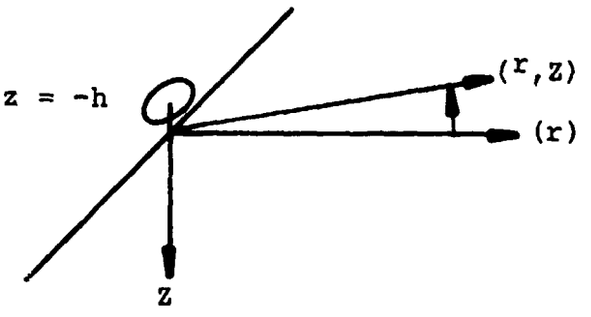

Figure D-1. Magnetic Dipole Geometry.

The quasistatic solution for the Hertz potential for a magnetic dipole can be written in the form:

$$\Gamma = \frac{m}{4\pi} \left[\frac{1}{R_0} + P \right]$$

where

$$P = \int_0^\infty \frac{u_e - \lambda}{u_e + \lambda} J_0(\lambda r) e^{-\lambda(h - z)} \, d\lambda$$

$$R = (r^2 + (z - h)^2)^{\frac{1}{2}} \tag{D.1}$$

and λ is a variable of integration and for M layers (Wait, 1962), u_e is:

$$u_e = u_1 \frac{Z_2/K_1 + \tanh u_1 h_1}{1 + Z_2/K_1 \tanh u_1 h_1} \tag{D.2}$$

where:

$$u_m = (\lambda^2 + \gamma_m^2)^{\frac{1}{2}} \qquad m = 0,1,2,3 \cdots M \tag{D.3}$$

$$\gamma_m^2 = (i\sigma_m \mu_m \omega - \varepsilon_m \mu_m \omega^2) \simeq i\sigma_m \mu_m \omega \tag{D.4}$$

for $\sigma_m >> \varepsilon_m \omega$.

$$Z_m = K_m \frac{Z_{m+1} + K_m \tanh u_m h_m}{K_m + Z_{m+1} \tanh u_m h_m} \qquad (D.5)$$

- -

$$Z_{M-1} = K_{M-1} \frac{K_M + K_{M-1} \tanh u_{M-1} h_{M-1}}{K_{M-1} + K_M \tanh u_{M-1} h_{M-1}}$$

and

$$K_m = \frac{u_m}{\sigma_m + i\omega\varepsilon_m} \simeq \frac{u_m}{\sigma_m} \simeq \frac{\gamma_m}{\sigma_m} \qquad (D.6)$$

and h_m is the thickness of the $m^{\underline{th}}$ slab.

The major contribution to the integral P in (E1) occurs for values of λ of the order of $|\gamma_0|$. Thus, for $|\gamma_m| >> |\gamma_0|$, equation (D.3) becomes:

$$u_m = (\lambda^2 + \gamma_m^2)^{\frac{1}{2}} \simeq \gamma_m \qquad (D.7)$$

To this order of approximation

$$u_e \simeq (\lambda^2 + \gamma_e^2)^{\frac{1}{2}} \simeq \gamma_e \qquad (D.8)$$

and

$$\gamma_e \simeq \gamma_1 \left\{ \frac{(Z_2/K_1) + \tanh u_1 h_1}{1 + (Z_2/K_1) \tanh u_1 h_1} \right\} \qquad (D.9)$$

We now follow closely Wait's (1969) analysis to determine the image approximation to the Hertz potential Γ.

Consider the Maclaurin series expansion of the expression:

$$f(\lambda) = e^{\alpha\lambda} \frac{u_e - \lambda}{u_e + \lambda} = \sum_{m=0}^{\infty} a_m \lambda^m \tag{D.10}$$

where α is to be determined and,

$$a_m = \frac{1}{m!} f^{(m)}(0) \tag{D.11}$$

Carrying out the derivative operations, we find that

$$f'(\lambda) = e^{\alpha\lambda} \frac{(u_e - \lambda)^2}{\gamma_e^2} \left\{\alpha - \frac{2}{u_e}\right\} \tag{D.12}$$

$$f''(\lambda) = f'(\lambda) \left\{\alpha - \frac{2}{u_e}\right\} + 2f(\lambda)\frac{\lambda}{u_e^3} \tag{D.13}$$

etc. By choosing $\alpha = 2/\gamma_e$ we find that $a_0 = 1$, $a_1=0$, $a_2=0$, $a_3=\left(\frac{\alpha}{2}\right)^3 \frac{2}{3!}$, $a_4=0$, $a_5= -\left(\frac{\alpha}{2}\right)^5 18/5!$, $a_6=\left(\frac{\alpha}{2}\right)^6 40/6!$, etc.

Thus:

$$\frac{u_e - \lambda}{u_e + \lambda} = e^{-\alpha\lambda}\left(1 + \left(\frac{\alpha}{2}\right)^3 \left(\frac{2\lambda}{3!}\right)^3 + \cdots\right) \tag{D.14}$$

and:

$$P = + \int_0^{\infty} (1 + \frac{\alpha}{2} \frac{2\lambda^3}{3!} + \cdots) J_0(\lambda p) e^{-\lambda(\alpha - z + h)} \tag{D.15}$$

$$= - \left(1 - \frac{\alpha}{2}^3 \frac{2}{3!} \frac{\partial^3}{\partial z^3} + \cdots\right) \frac{1}{R_a}$$

where $R_a = (r^2 + (h + \alpha - z)^2)^{\frac{1}{2}}$ (D.16)

For $\sigma_m >> \varepsilon_m \omega$ and $\mu_0 = \mu_m$ for all m, we can represent α as:

$$\alpha = 2\gamma_e \simeq \delta_1 (1 - j) \frac{\tanh\left\{(1+j)\frac{h_1}{\delta_1}\right\} + R_1 \frac{\delta_2}{\delta_1}}{1 + R_2 \frac{\delta_3}{\delta_2} \tanh\left\{(1+j)\frac{h_1}{\delta_1}\right\}} \qquad (D.17)$$

where:

$$R_1 = \frac{\tanh\left\{(1+j)\frac{h_2}{\delta_2}\right\} + R_2 \frac{\delta_3}{\delta_2}}{1 + R_2 \tanh\left\{(1+j)\frac{h_2}{\delta_2}\right\}} \qquad (D.18)$$

and:

$$R_{M-1} = \frac{\tanh\left\{(1+j)\frac{h_M}{R_M}\right\} + R_M \frac{\delta_{M+1}}{\delta_M}}{1 + R_M \frac{\delta_{M+1}}{\delta_M} \tanh\left\{(1+j)\frac{h_M}{\delta_M}\right\}} \qquad (D.19)$$

For the two layer case, $h_2 \to \infty$ and $\delta_3 \to \delta_2$. Thus:

$$R_1 \to \frac{1 + R_2}{1 + R_2} = 1 \qquad (D.20)$$

and:

$$\alpha = \delta_1 (1-j) \frac{\tanh\left\{(1+j)\frac{h_1}{\delta_1}\right\} + \frac{\delta_2}{\delta_1}}{1 + \frac{\delta_2}{\delta_1} \tanh\left\{(1+j)\frac{h_1}{\delta_1}\right\}}$$

As shown in Chapter 4, we can write:

$$H_r = \frac{\partial^2 \Gamma}{\partial z^2} \tag{D.21}$$

and

$$H_z = \frac{\partial^2 \Gamma}{\partial z^2} \tag{D.22}$$

Retaining only the first term of the Maclaurin series expansion in equation (D.15) and normalizing the magnetic fields by multiplying H_r and H_z by $4\pi r^3/m$, we find expressions for the normalized "image" fields near the surface to be:

$$H_r \cong \frac{3z}{r} - \frac{3(\alpha/r)}{\{1 + (\alpha/r)^2\}^{5/2}} + \text{H.O.T. (neglected)} \tag{D.23}$$

$$H_z \cong 1 - \frac{2(\alpha/r)}{\{1 + (\alpha/r)^2\}^{5/2}} + \text{H.O.T. (neglected)} \tag{D.24}$$

Noting that the higher order neglected terms contain expressions of the form (I):

$$I = \sum_{n>5}^{\infty} \beta_m \, (1 + (\alpha/r)^2)^{-m/2} \tag{D.25}$$

we can readily deduce that equations (D.23) and (D.24) are accurate descriptions of the magnetic field intensities only for ranges large with respect to the real part of α, i.e., r>>Real α. Graphically comparing the expressions for the "image" fields with those of the exact integral fields for the H_r component (Figure D-2), we note that, when the source is on or near the surface of the earth, the image formulation for the magnetic field near the surface is accurate within 10% only for $r > 7\ \mathrm{Re}|\alpha|$ and is not of much practical use in our application.

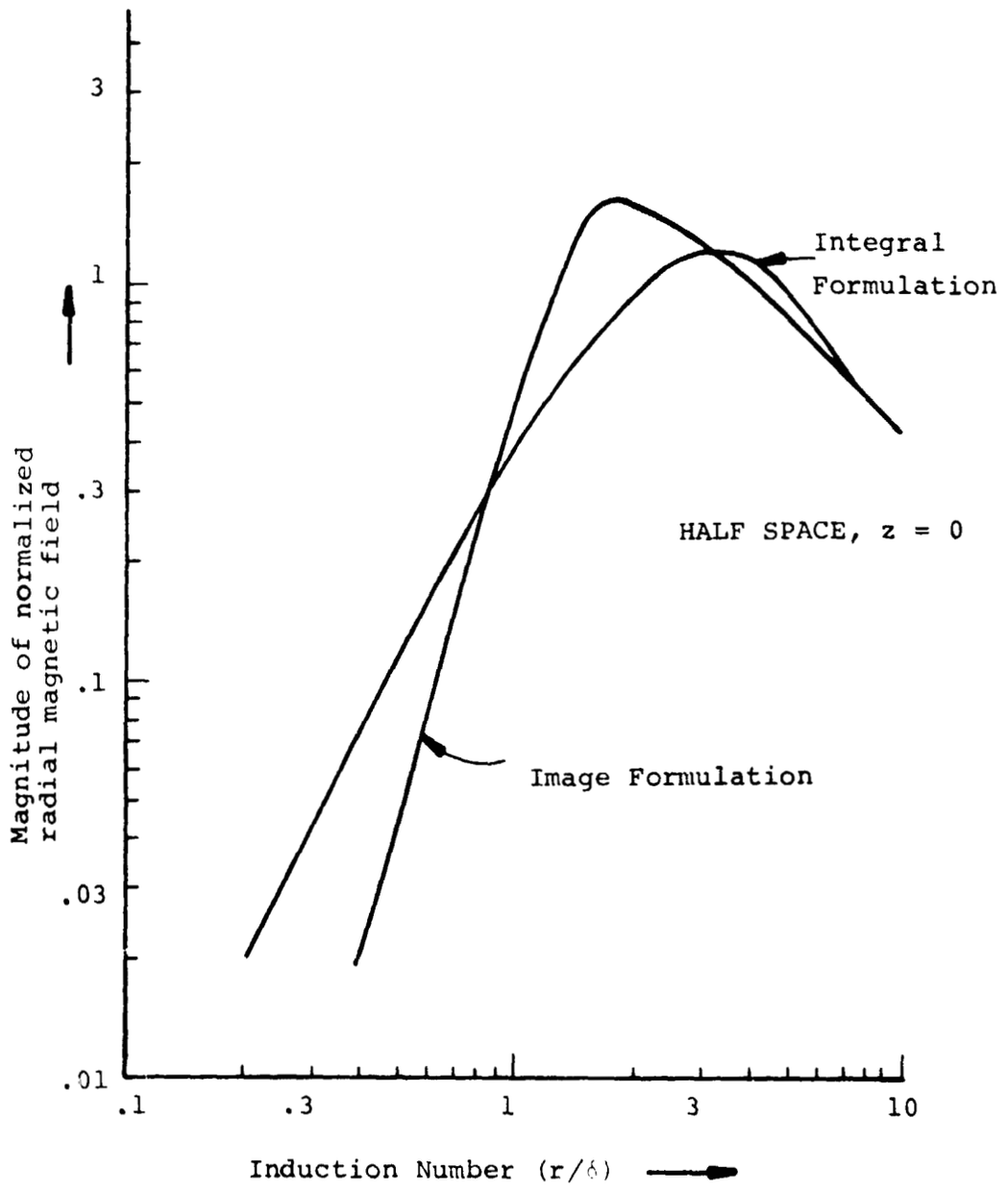

Figure D-2. Comparison of H_r for Integral and Image formulations.

Appendix E: Switched Source Synthesizer

A practical implementation of the SWEEP inductive coupling geophysical prospecting technique requires that the source magnetic field be generated with a physically small coil that can be deployed easily or, preferably, can be mounted permanently on a small vehicle. But, to permit examination of strata to depths of the order of a few hundred meters we must use a source with a magnetic moment of the order of 10^4 amperes-turns-meters^2. Practically, we need currents of the order of 50 amperes and power of the order of 15 kilowatts.

For some time now work has been proceeding on the development of an all solid state high power DC-to-AC inverter for another application which also happens to require currents and powers of this order. And this work has led to the development of novel techniques[1] which allow highly efficient syntheses of various waveforms, including sinusoids, directly from storage batteries.

The concept for the switched source synthesizer is shown in Figure E-1. The configuration allows various combinations of batteries to be connected sequentially in series to generate a time varying voltage. In the illustration, the battery voltages are $V_p/2$, $V_p/3$, and $V_p/6$, respectively, and when the batteries are connected in a proper time sequence, the arrangement generates a quasisinusoidal waveform as shown in Figure E-2.

---

(1) R.H. Baker and L.H. Bannister, "Electric Power Converter", Patent Pending.

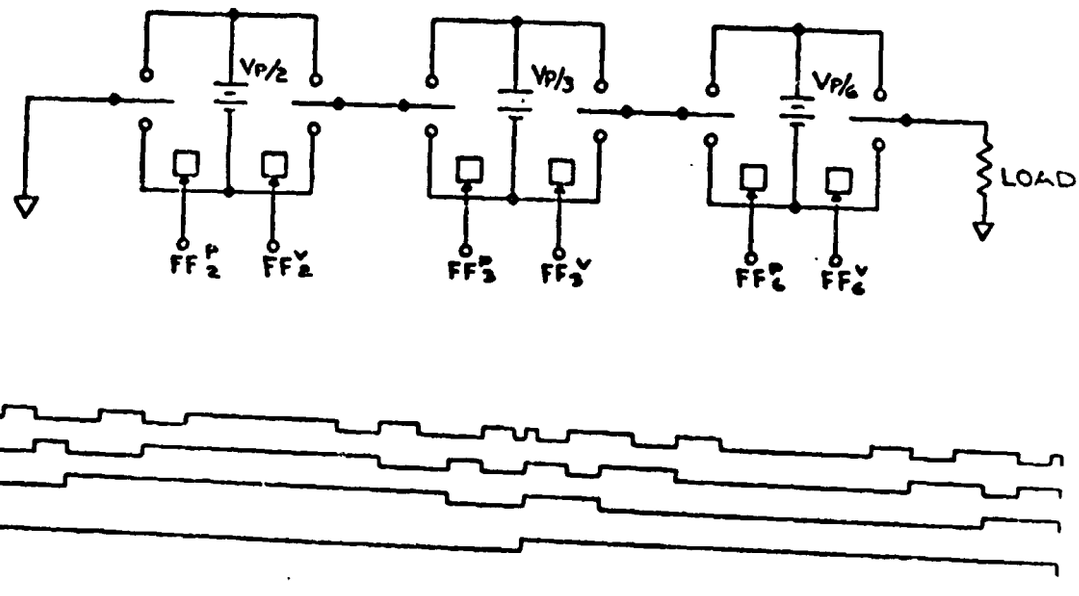

Figure E-1

Concept of Switched Source Synthesizer Used for Generation of Quasisinusoid.

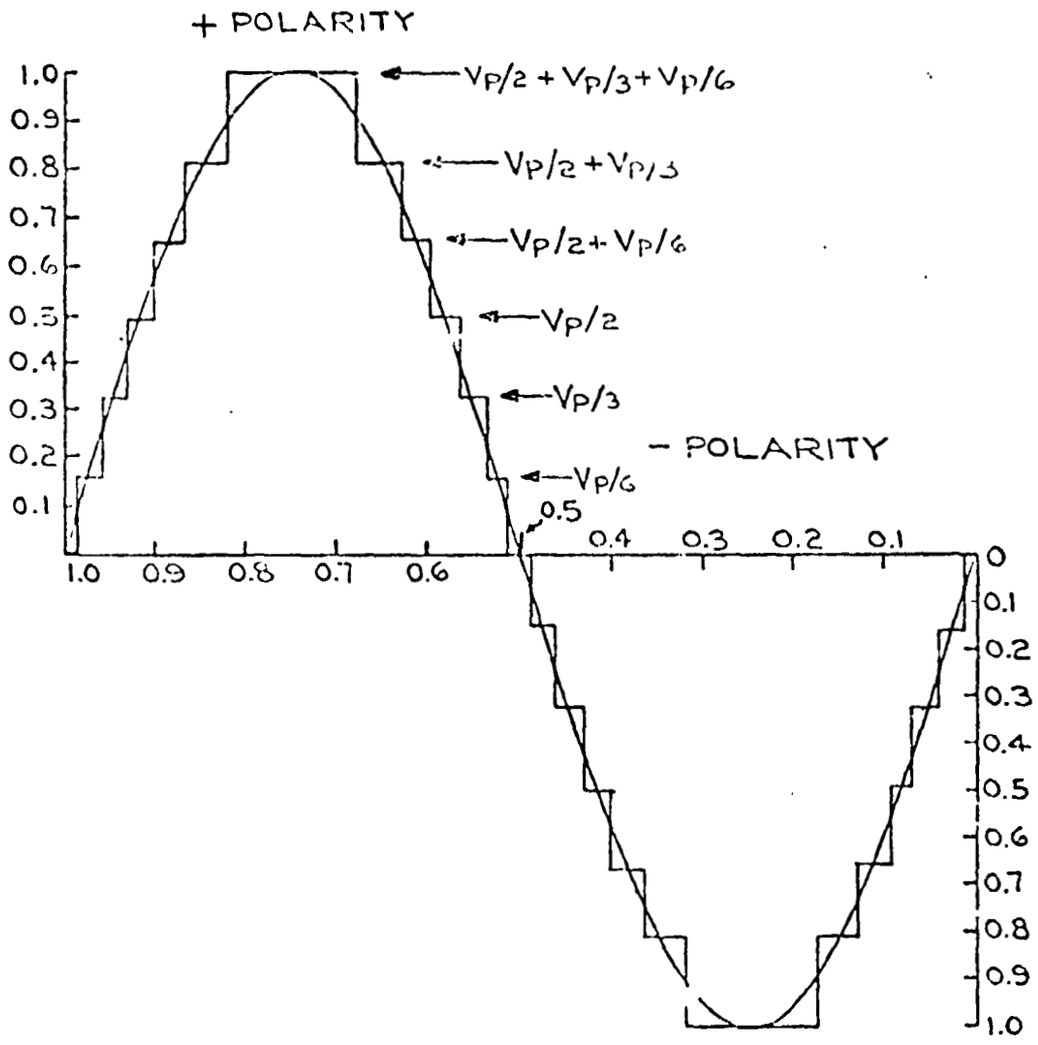

Figure E-2

Six-step Approximation to a Sinewave

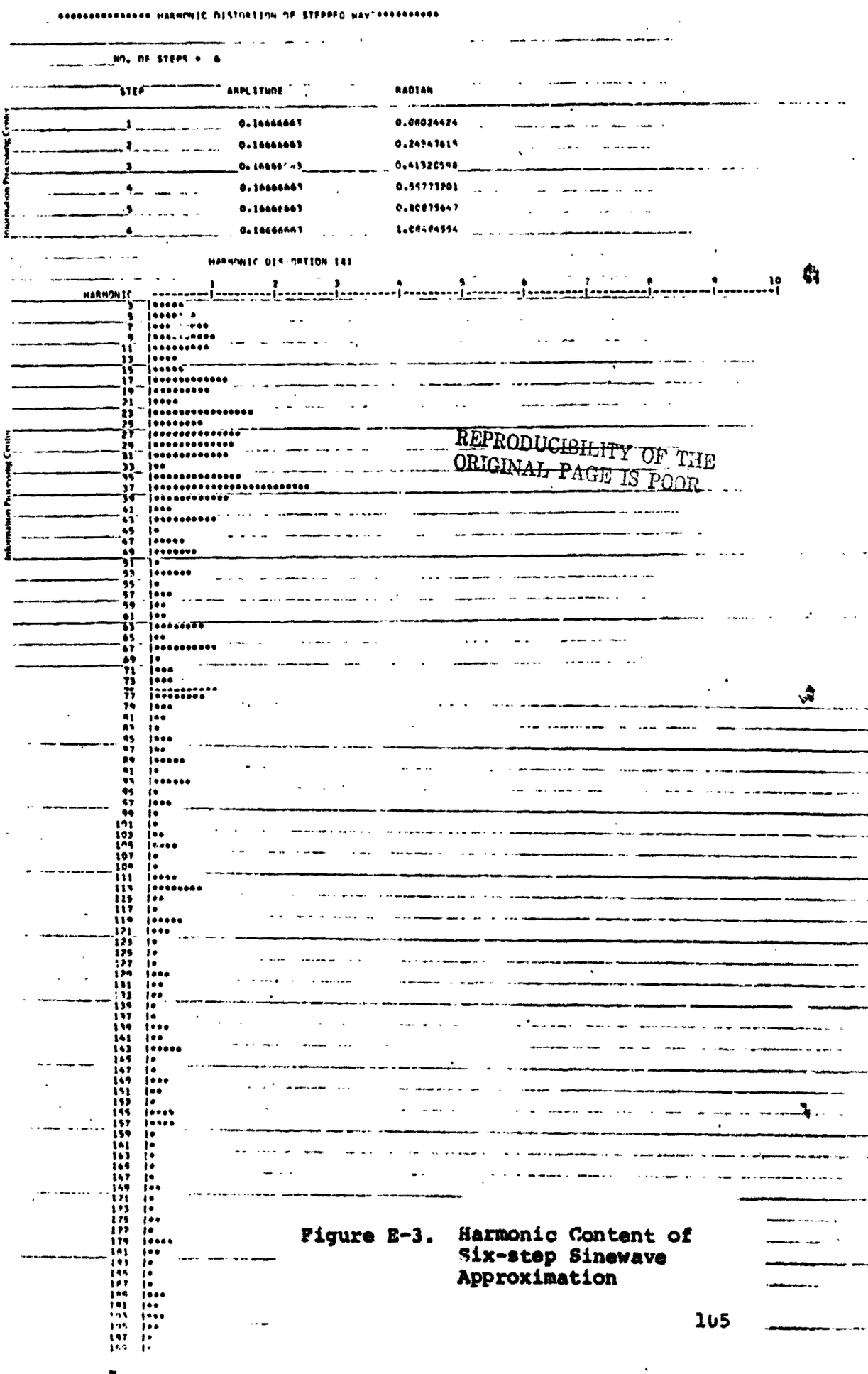

Figure E-3. Harmonic Content of Six-step Sinewave Approximation

There are several interesting technical features of a switched source synthesizer that make it quite attractive as a DC to AC inverter:

a. For the sinusoidal waveform shown in Figure E-2, not only is the total harmonic distortion small (6%), but in addition, the major components of distortion are concentrated at the higher harmonic frequencies. Figure E-3 shows the relative magnitude of the various harmonic components for a six-step sinusoidal approximation. The largest component of distortion (3%) occurs at the 35^{th} harmonic which is easy to filter from the fundamental.

b. Any frequency from near zero to several kilohertz can be generated with constant amplitude and harmonic distortion because the inverter does not use a transformer.

c. The switched source synthesizer is inherently efficient because it is a nonlinear system and the transistor switches are never operated in the linear region of simultaneous high voltage and high current. This high power efficiency (η>95%) allows circuit packaging in compact form which in turn leads to light weight portable equipment.

We believe that the switched source synthesizer configuration combines the features of portability, high efficiency, and low harmonic distortion over a wide frequency range, which make it an almost ideal source for our SWEEP inductive coupling geophysical probing technique.